Published in final edited form as:
J Geophys Res Planets. 2016 July ; 121(7): 1293–1320. doi:10.1002/2015JE004924.

The complex relationship between olivine abundance and thermal inertia on Mars

Romy D. Hanna[1], **Victoria E. Hamilton**[2], and **Nathaniel E. Putzig**[2,3]

[1]Jackson School of Geological Sciences, University of Texas at Austin, Austin, Texas, USA

[2]Department of Space Studies, Southwest Research Institute, Boulder, Colorado, USA

[3]Now at the Planetary Science Institute, Lakewood, Colorado, USA

Abstract

We examine four olivine-bearing regions at a variety of spatial scales with thermal infrared, visible to near-infrared, and visible imagery data to investigate the hypothesis that the relationship between olivine abundance and thermal inertia (i.e., effective particle size) can be used to infer the occurrence of olivine chemical alteration during sediment production on Mars. As in previous work, Nili Fossae and Isidis Planitia show a positive correlation between thermal inertia and olivine abundance in Thermal Emission Spectrometer (TES) and Thermal Emission Imaging System (THEMIS) data, which could be interpreted as indicating olivine chemical weathering. However, geomorphological analysis reveals that relatively olivine-poor sediments are not derived from adjacent olivine-rich materials, and therefore, chemical weathering cannot be inferred based on the olivine-thermal inertia relationship alone. We identify two areas (Terra Cimmeria and Argyre Planitia) with significant olivine abundance and thermal inertias consistent with sand, but no adjacent rocky (parent) units having even greater olivine abundances. More broadly, global analysis with TES reveals that the most typical olivine abundance on Mars is ~5–7% and that olivine-bearing (5–25%) materials have a wide range of thermal inertias, commonly 25–600 J m^{-2} K^{-1} $s^{-1/2}$. TES also indicates that the majority of olivine-rich (>25%) materials have apparent thermal inertias less than 400 J m^{-2} K^{-1} $s^{-1/2}$. In summary, we find that the relationship between thermal inertia and olivine abundance alone cannot be used in infer olivine weathering in the examined areas, that olivine-bearing materials have a large range of thermal intertias, and therefore that a complex relationship between olivine abundance and thermal inertia exists on Mars.

1. Introduction

Surfaces on Mars having bulk mineralogies (determined from orbital spectroscopy) dominated by plagio-clase, pyroxene, and olivine have been characterized as basaltic and assumed to be relatively unaltered [e.g., *Bandfield et al.,* 2000a; *Rogers and Christensen,* 2007]. In localized areas, some of these generally basaltic surfaces have been identified as containing relative enrichments of olivine [*Hamilton etal.,* 2003; *Hoefen etal.,* 2003]. Although these olivine-enriched areas have been cited as evidence that there has not been extensive aqueous alteration on the Martian surface [e.g., *Stoparetal.,* 2006], unknown

Correspondence to: R. D. Hanna, romy@jsg.utexas.edu.

abundances of hydrous phases have been identified in proximity to them [e.g., *Ehlmann et al.,* 2009]. In addition, there is evidence for the limited and localized presence of minerals indicative of at least intermittent periods of chemical alteration due to the presence of fluids in several other locations on Mars [e.g., *Squyres et al.,* 2004; *Bibring et al.,* 2005; *Ming et al.,* 2006; *Mustard et al.,* 2008; *Ehlmann et al.,* 2009; *Ehlmann and Edwards,* 2014; *Bristow et al.,* 2015]. Further, chemical models and documented chemical trends may indicate that virtually all surface materials observed via orbital spectroscopy have undergone some small amount of alteration/weathering [e.g., *Hurowitz et al*., 2006; *McSween et al*., 2009].

Several of the most intensively studied regions of relative olivine enrichment determined via orbital spectroscopy occur in association with units having relatively high thermal inertia (e.g., $>500 Jm^{-2}K^{-1} s^{-1/2}$), consistent with high rock abundance, indurated, or cemented materials [e.g., *Nowicki and Christensen,* 2007; *Piqueux and Christensen,* 2009; *Hamilton et al.,* 2014]. These include materials near the Nili Fossae [*Hamilton et al.,* 2003; *Hoefen et al.,* 2003; *Hamilton and Christensen,* 2005], Isidis Planitia [*Hamilton et al.,* 2003; *Tornabene et al.,* 2008], and Argyre Planitia [*Hamilton et al.,* 2003; *Koeppen and Hamilton,* 2008]. In one localized study, detailed examination of the mineralogies of materials in Argyre Planitia showed relatively olivine-enriched outcrops surrounded by relatively olivine-poor, low inertia sediments, and this relationship was interpreted as suggesting that olivine is preferentially eroded out of rocky materials as they are converted to sediments/soils [*Bandfield and Rogers,* 2008]. Those investigators hypothesized that relations like these may be prevalent globally, which would suggest that Martian dark regions may be composed of materials that once contained greater abundances of olivine than they do today and thus do not represent primary igneous compositions. *Bandfield et al.* [2011] explored this hypothesis in more detail using Thermal Emission Imaging System (THEMIS) imagery for olivine-bearing areas around the Nili Fossae and in southern Isidis Planitia. Using modeled olivine abundances from THEMIS daytime infrared images and thermal inertia (as a proxy for particle size) derived from overlapping THEMIS nighttime temperature images, they observed a qualitative correlation between thermal inertia and olivine abundance for both areas. On the basis of these two areas and mini-Thermal Emission Spectrometer (mini-TES) observations of olivine-poor sediment relative to more olivine-bearing rock in Gusev crater, they concluded that chemical alteration of olivine was occurring in the course of sediment production and further that “most Martian dark regions have likely experienced aqueous alteration” [*Bandfield et al.,* 2011].

The interpretation that most Martian sediments lack olivine due to chemical weathering relies on several assumptions about both the data sets used and Martian geology that may not be correct. For example, one assumption is that thermal inertia essentially represents surfaces having relatively homogeneous particle sizes, and although this may be a reasonable assumption in many localities, it is certainly not the case everywhere on Mars. Mixtures and/or layering of materials with two or more sets of properties (e.g., grain size, albedo, and porosity) can produce values of apparent thermal inertia comparable to homogeneous materials with an entirely different set of properties [*Jakosky,* 1979; *Putzig and Mellon,* 2007a, 2007b]. In terms of the geology, if we postulate that a positive correlation between thermal inertia and olivine abundance globally is the result of chemical alteration of olivine, we are inherently assuming that virtually all present sediments were

derived from bedrock that is olivine bearing; i.e., they could not have come from olivine-poor rocks. We should consequently expect that materials having high inertia have relatively high olivine abundances (i.e., there cannot be high inertia materials with low olivine abundances). Yet another assumption is that none of the high inertia materials we observe today are secondary lithologies (i.e., lithified sedimentary rock like that observed at Meridiani and Gale Crater [*Squyres and Knoll,* 2005; *McLennan et al.,* 2014]). It is likely that all of these are unrealistic assumptions on global, regional, and potentially local scales

When using the correlation between thermal inertia and olivine abundance to infer chemical weathering of olivine, an additional, critical assumption is that the lower inertia materials are a direct weathering product of nearby, higher inertia materials. And we have to assume that no other geologic processes (e.g., mixing and embayment) are acting on the materials we are investigating. Detailed geomorphological analysis of the exposed surfaces within an area is therefore necessary to verify that the evaluated materials are geologically related from a weathering perspective. If the materials are found to be geologically unrelated, a positive correlation between olivine abundance and thermal inertia cannot be used to infer chemical weathering of olivine.

If the above assumptions are not valid, then the correlation between thermal inertia and olivine abundance, even if positive, cannot be used (in the absence of other analyses) to infer the occurrence of olivine chemical alteration during sediment production on Mars. In other words, positive correlation is not sufficient to infer causation. In this work we build on prior studies by investigating whether there is evidence for chemical alteration of olivine-bearing Martian surface materials by examining the relationship of olivine abundance and thermal inertia and including geomorphological data. We first examine the thermal inertia of olivine-bearing materials on a global scale with the Thermal Emission Spectrometer (TES) to determine the nominal range of olivine abundances and their apparent thermal inertias. Then we thoroughly examine the relationship between spatially correlated thermal inertia and olivine abundance using TES and THEMIS for four olivine-bearing regions. We investigate previously examined regions, plus explore an additional area, at a broader range of scales than prior studies, combining observations from TES, THEMIS, the European Space Agency Mars Express Observatoire pour la Minéralogie, l'Eau, les Glaces, et l'Activité (OMEGA), the NASA Mars Reconnaissance Orbiter Compact Reconnaissance Imaging Spectrometer for Mars (CRISM), and the Context Camera (CTX) and High Resolution Imaging Science Experiment (HiRISE) instruments on board the Mars Reconnaissance Orbiter. Further, we carefully examine the geological relationships of units and sediment exposed in the examined areas to verify the assumptions inherent in this type of analysis and to test the hypothesis that a positive correlation between thermal inertia and olivine abundance can be used to infer chemical alteration of olivine.

2. Data and Methods

2.1. Thermal Emission Spectrometer Mineralogy and Thermal Inertia Data

The Thermal Emission Spectrometer (TES) on the Mars Global Surveyor spacecraft is a hyperspectral thermal infrared spectrometer that collects spectra between ~1650 and 200cm^{-1} (~6–50μm) for a roughly 3 ×6 km area on Mars [*Christensen et al.,* 2001b]. In the

thermal infrared (TIR), surface scattering dominates the reflected infrared energy of mineral grains causing the reflected TIR spectra of mineral phases to combine linearly in proportion to their abundance (in contrast to the visible/near-infrared wavelength region where volume scattering dominates leading to nonlinearity in spectral mixtures) [*Lyon*, 1964; *Thomson and Salisbury,* 1993]. Therefore, the modal mineralogy of a complex mineral assemblage can be determined by linearly modeling its TIR spectrum with an end-member library of candidate mineral spectra [*Ramsey and Christensen,* 1998; *Feely and Christensen,* 1999; *Hamilton and Christensen,* 2000]. *Koeppen and Hamilton* [2008] modeled global mineralogy, including olivine abundance, from a linear least squares model of TES spectral data; we used the olivine abundances derived from that study for analyses at global to regional scales. In specific cases we retrieved the original TES data and model them using a nonnegative least squares fitting algorithm [*Rogers and Aharonson,* 2008] and the end-member library of *Rogers and Bandfield* [2009], with the addition of four olivine spectra (Fo_{18}, Fo_{25}, Fo_{39}, and Fo_{53}) from *Koeppen and Hamilton* [2008]. Phases in the library included the following: quartz, feldspars, pyroxenes, olivines, phyllosilicates, amorphous silica, amphiboles, hematite, sulfates, carbonates, and zeolites. We report normalized abundances that represent the total fraction of surface materials, excluding the contributions of atmospheric components. These data represent dust-free to slightly dusty surfaces (Lambert albedo, <0.20) meeting specific spectral data quality constraints that minimize atmospheric contributions and maximize data quality from TES orbit numbers (OCKs) 1583–8000 [*Koeppen and Hamilton,* 2008]. (Spectral data acquired after roughly OCKs 7000–8000 suffer from increased microphonic noise attributable to vibration of the aging Mars Global Surveyor spacecraft so are not used for full wavelength range analyses [*Bandfield,* 2002; *Hamilton et al.,* 2003].) To further constrain the data selection to the least dusty surfaces to ensure accurate modeling of surface composition, we used the dust cover index (DCI) of *Ruff and Christensen* [2002], selecting data with DCI values of >0.962. Due in part to the narrowness and spectral contrast of olivine features, the minimum abundances required for the detection of olivine in TES data are somewhat lower than for many minerals, with derived olivine abundances of as low as 5% being considered reliable detections [*Koeppen and Hamilton,* 2008].

The thermal bolometer subsystem of TES is used to derive the thermal inertia of the same surface area for which a thermal infrared spectrum is collected [*Christensen et al.,* 2001b]. Thermal inertia is a measure of a material's ability to absorb and retain heat, and thermal inertia values of Martian surfaces are dominated by physical properties such as particle size and porosity in the upper few centimeters of the surface [*Putzig and Mellon,* 2007a]. For the majority of this work we used the daytime bolometer-derived thermal inertia of *Mellon etal.* [2000] which is the currently available data set in the Planetary Data System (PDS). The uncertainty of daytime results can be several times that of nighttime results [*Putzig and Mellon,* 2007b] due to errors in albedo, but for this study using concurrent bolometer and spectrometer observations is of greater priority to ensure geographic correspondence. However, we did verify that using TES nighttime thermal inertia (from the binned median data product of *Putzig and Mellon* [2007b]) did not significantly change our results for one of the examined regions (Nili Fossae). We also used the updated thermal inertia values calculated by *Putzig and Mellon* [2007b] in the course of evaluating unusual trends in the

thermal inertia data and to check for seasonal effects; the version of the thermal inertia data does not have a noteworthy impact on our results, as described below.

2.2. Thermal Emission Imaging System Composition and Thermal Inertia Data

The Thermal Emission Imaging System (THEMIS) is a visible and thermal infrared multispectral imaging system on board the 2001 Mars Odyssey spacecraft [*Christensen etal.,* 2003]. We utilize data from the IR imaging subsystem, which collects ~32 km wide images at nine wavelengths between ~1475 and 667cm^{-1} (6.78–15 μm) at a spatial resolution of ~100 m/pixel [*Christensen et al.,* 2004]. We selected daytime THEMIS images for compositional analysis on the basis of their location over regions of interest and the indication of the presence of olivine based on its distinctive purple to bluish color in decorrelation stretched (DCS) images using THEMIS bands 8, 7, and 5 [e.g., *Gillespie et al.,* 1986; *Hamilton and Christensen,* 2005]. There is insufficient analysis in the literature demonstrating the accuracy of thermal inertia derived from THEMIS daytime imaging, so we used THEMIS nighttime (band 9, 795.5 cm^{-1}, 12.57 μm) images for thermal inertia derivation, selecting specific images to maximize the area of overlap with the corresponding daytime compositional images [*Fergason et al,* 2006].

We derived olivine abundance from daytime THEMIS images using the method detailed in *Bandfield et al.* [2004]. Briefly stated, we derived the surface emissivity for the entire image by selecting a “training region” of sufficient size (minimum 50×50 pixels) within the image that appears spectrally homogenous. We used a TES-derived surface spectrum for the area to determine the atmospheric contribution during THEMIS data acquisition and remove this contribution from the entire image. The TES-derived spectrum was either high-albedo surface (dust) [*Bandfield and Smith,* 2003] or Surface Type 1 [*Bandfield et al.,* 2000a]. In all cases we confirmed that the TES surface spectrum provided a good model fit to retrieved TES spectra over the training region by modeling a spectral average of the retrieved TES spectra with four TES-derived surface spectra that have been shown to be characteristic of most Martian dark regions: Surface Type 1, Surface Type II, high-albedo surface (dust), and a hematite-rich basaltic surface [*Bandfield et al.,* 2000a; *Christensen et al.,* 2001a; *Bandfield and Smith,* 2003]. A good model fit was evaluated based on a low RMS error as well as visual confirmation that the modeled TES surface spectrum was a good fit to the averaged, retrieved TES spectrum. Two assumptions are inherent in the THEMIS atmospheric correction: (1) the surface composition of the training region is known and homogenous within the defined area and (2) the atmosphere contributions to the observed spectral radiance are similar over the entire image (i.e., there are no large topographic variations or locally variable atmospheric phenomena) [*Bandfield et al.,* 2004]. Because the atmospheric correction algorithm cannot account for variable atmospheric features such as water ice clouds, we used a water ice spectrum during the surface spectrum modeling step (see below) if we suspect them to be present within the image (i.e., if water ice is modeled at significant amounts, we retain it as a model end-member for all later model runs but remove it from the end-member set otherwise) [*Bandfield et al.,* 2004].

Once the THEMIS image has been converted to surface emissivity, we used a nonnegative linear least squares algorithm [*Rogers and Aharonson,* 2008] with four or five end-members

to model bands 3–9 (7.93 μm, 8.56 μm, 9.35 μm, 10.21 μm, 11.04 μm, 11.79 μm, and 12.57 μm). Linear modeling requires that the number of end-members be less than or equal to the number of channels, so we used scene-derived end-members (a common terrestrial remote sensing analysis approach) to ensure that we represent what is actually present, even if the end-member is a mixture [*Bandfield et al.,* 2004]. Specifically, we used a scene-derived, olivine-bearing spectrum instead of a laboratory olivine spectrum to accurately capture all olivine in the scene. In all cases we confirmed the olivine signature by observing a band minimum at ~11 μm in the scene-derived spectrum [e.g., *Hamilton and Christensen,* 2005]. We also derived end-members for basalt and high-silica lithologies from the scene, and additional end-members included the TES-derived, high-albedo (dust) shape [*Bandfield and Smith*, 2003], a blackbody spectrum to account for variable spectral contrast, and a TES-derived, water ice spectrum [*Bandfield et al.,* 2000b]. For the scene-derived end-members we averaged the spectra in a small (~100–500 square pixel) spectrally homogenous area of interest within the THEMIS image after atmospheric correction. All end-member concentrations presented in this work have been normalized to remove the water ice component, if it was modeled. We note that THEMIS-derived olivine abundances represent olivine-bearing material and not a pure olivine component; therefore, the actual absolute olivine abundance is lower than the reported value but relative olivine abundances are not expected to change significantly.

We produced THEMIS thermal inertia images on a per pixel basis using nighttime band 9 (12.57 μm) brightness temperature (assumed to represent surface temperature) as a “one-point” mode input to the KRC thermal model [*Kieffer,* 2013]. The other inputs we specified for the model were latitude and longitude (center of overlap for the day and nighttime images), the local solar time and solar longitude of the image observation, and dust visible opacity. Because the visible opacity is approximately twice the IR opacity [e.g., *Martin,* 1986; *Kieffer,* 2013], to derive this value, we located a daytime THEMIS image close to the time of observation of the nighttime image (within approximately 25 orbits), recorded the daytime dust IR opacity, and then doubled this value for input into the KRC model.

2.3. Other Spectral and Imaging Data Sets

In addition to TES and THEMIS, we used high-resolution visible imagery and visible to near-infrared (VNIR) spectral data from Mars Express and Mars Reconnaissance Orbiter missions. We utilized global spectral parameter maps produced from the OMEGA and CRISM instruments to survey several areas for the presence of olivine in the VNIR spectral region in order to confirm TIR spectral region olivine detections or to determine the presence of olivine in areas where TIR data are unavailable. The OMEGA team has created three spectral index maps created for olivine, OSP1, OSP2, and OSP3, which are all sensitive to the presence of olivine (in abundances as low as 5–10% depending on the index used [*Ody et al,* 2013]). These indices are optimized for the following: (1) the detection of low iron content and/or small grain size and/or low abundance (OSP1), (2) higher iron content and/or larger grain size and/or higher abundance (OSP2), and (3) olivine in areas of higher amounts of aerosols and/or dust cover (OSP3) [*Ody et al.,* 2012, 2013]. The CRISM team has derived a spectral index to detect the presence of olivine (OLINDEX2), which is available from the PDS as 5°×5° map tiles at a resolution of 256 ppd (230 m/pixel) [*Pelkey*

et al., 2007; *Salvatore et al.,* 2010; *Viviano-Beck et al.,* 2014]. For visible imagery, we utilized data from the CTX and HiRISE instruments on board the Mars Reconnaissance Orbiter [*Malin et al.,* 2007; *McEwen et al.,* 2007]. All of these data sets were manipulated and analyzed using the JMARS software package [*Christensen et al,* 2009].

2.4. Examination of Olivine Abundance and Thermal Inertia Relationships

For the global and regional analyses with TES we plotted thermal inertia and olivine abundance on a per point basis (i.e., density cloud) to assess the relationship between olivine abundance and thermal inertia. However, density slicing the data (i.e., partitioning the data into defined intervals) has the advantage that it minimizes the effects of point-to-point noise and also allows for a simplified presentation of the relationship (i.e., possible correlation) between thermal inertia and olivine abundance. Because surfaces within relatively smaller areas are ostensibly geologically related (compared to the global scale where this is certainly not true), for regional and local analyses we binned the thermal inertia detections falling within a particular thermal inertia range (i.e., density sliced on thermal inertia) and calculated the average olivine abundance for each bin. We found that this approach was particularly useful for THEMIS local analyses, where the low number and scene-derived nature of the end-members (three to five) resulted in modeling of olivine-bearing material (including 100%) across the scene and at a large variety of thermal inertias. This resulted in rather diffuse density plots that did not easily show trends and therefore were difficult to interpret. To define the thermal inertia bins, we used the maximum thermal inertia as the maximum of the first bin and defined the width of the bin as 20% of this maximum value. The maximum of the next bin was defined as the minimum of the previous bin and its width 20% of this value and so on, until the minimum value of the last bin was 50 J m^{-2} K^{-1} $s^{-1/2}$ or less. We chose the bin width as 20% of the maximum bin value because this is approximately twice the estimated average uncertainty (6–15%) in TES and THEMIS-derived thermal inertia [*Mellon etal.,* 2000; *Fergason etal.,* 2006]. Because we are using thermal inertia as the determinant for creating bins, bin widths smaller than the size of the thermal inertia measurement uncertainty may not represent unique thermal inertia units. We tried enlarging the width of the bins (i.e., bin widths larger than 20% of the maximum bin value), but this decreased the number of bins and often resulted in an insufficient number of data points to asses the relationship between thermal inertia and olivine content. Therefore, we made the bins as small as statistically possible (approximately double the measurement uncertainty) to create a sufficient number of thermal inertia units for each site. Further, we discarded any thermal inertia bin that contained less than 10 (TES) or 100 (THEMIS) observations to ensure that only thermal inertia bins with an adequate number of data points were considered in the examination of the olivine/thermal inertia relationship. Finally, we tested the approach of density slicing the derived olivine abundances into 10 equal width bins between 0 and 100% but found that it nearly always displayed the same relationship with the derived average thermal inertia (i.e., the results did not change).

Although the pixels from which TES-derived daytime thermal inertia and olivine abundance are colocated by design, the THEMIS-derived thermal inertia (nighttime) and olivine abundance (daytime) represent observations acquired at different times. We initially matched pixel locations between the two images by using the latitude and longitude values reported

for each image in the ISIS-derived projection but found that images were still slightly offset from each other. To more accurately align the data from the daytime and nighttime observations, we then coregistered the overlapping areas by matching three features in each image (usually small crater centers) and shifting the nighttime image to match the daytime one (the shifts required were a maximum of 1 to 3 pixels in latitude and longitude). As a final note, all of our data analysis is performed using unsmoothed THEMIS data, but for visualization purposes, we smoothed (by 3) all THEMIS end-member images (i.e., modeled basalt, dust, olivine, and high silica) shown in the figures.

3. Results

3.1. TES Global Data

We first examined the relationship between thermal inertia and normalized olivine abundance on a global scale using TES. A density plot of all TES data meeting our selection criteria is shown in Figure 1. It is immediately apparent that a simple, positive correlation between thermal inertia and olivine abundance is not present at this scale and that all thermal inertia surfaces have a wide range of olivine abundances. The most common (i.e., highest-density) thermal inertia surfaces are low to intermediate thermal inertias (100–400J m^{-2} K^{-1} $s^{-1/2}$). Figure 1 also indicates that while normalized olivine contents up to 50% are present on Mars, the most common olivine abundance is below 10%. What is also readily evident is the occurrence of discontinuities in the data density at constant values of thermal inertia (e.g., at ~170 and ~250J m^{-2} K^{-1} $s^{-1/2}$). The TES-derived thermal inertia presented in Figure 1 is from the ASU TES database and was derived following the method of *Mellon et al.* [2000]. Subsequent to that work, *Putzig and Mellon* [2007b] produced an updated and improved version of TES-derived thermal inertia, so we also plotted normalized olivine content versus the median daytime and nighttime TES thermal inertias from the global maps included in this later work to see if the density discontinuities were eliminated with the new derivation. The density discontinuities persisted, but the thermal inertia values at which they occur changed, confirming that the effect is independent of the thermal inertia model used.

In association with this study, we conducted an investigation into the cause of the data density discontinuities at constant values of thermal inertia (Figure 1). As noted above, the discontinuities occur at different values for thermal inertia derived from two different algorithms [*Mellon et al.,* 2000; *Putzig and Mellon,* 2007b]. The values at which the discontinuities occur correspond to the nodal values of thermal inertia that were used in the respective look-up tables used in the two derivation algorithms. At the same time, the TES temperature observations and the model temperatures in the look-up tables from which the thermal inertia is derived do not exhibit any discontinuities that might explain those found in the derived thermal inertia. In both cases, the nodes of thermal inertia in the look-up table are logarithmically spaced and the derivation algorithm performs a linear interpolation in the logarithm of thermal inertia. Because temperature is not strictly a function of the logarithm of thermal inertia, any interpolation method will introduce errors in derived values between the interpolation nodes, and the choice of interpolation method may skew the results toward one node. We investigated the use of a spline interpolation as suggested by H. H. Kieffer (personal communication, 2010), but this alternative method had only a very minor effect on

the distribution of thermal inertia between the nodes in the look-up table. In general, we found that different interpolation methods yielded somewhat different magnitudes and senses of discontinuity, but no available interpolation method proved able to eliminate the discontinuities, which are inherent to the nonlinear relationship between temperature and thermal inertia and the use of interpolation—regardless of method—between relatively coarsely spaced nodes. In future work, the discontinuities could be greatly suppressed with a sub-stantially finer node spacing, which should now be possible with computational advances that have occurred since the development of the TES derivation algorithms. It is important to take note of the fact that the discontinuities may be much larger (by 1 or more orders of magnitude) if the input data are restricted to the lowest values of the thermal inertia quality flag in the TES database (i.e., the highest-quality data). The quality flag is set in the TES derivation algorithm on the basis of the absolute derivative of the logarithm of thermal inertia with respect to temperature as calculated between the nodes of the look-up table. Larger values of the derivative, which yield higher values of the quality flag, tend to occur much more frequently between the nodes due to the nonlinear relationship between the logarithm of thermal inertia and temperature.

Because the discontinuity is not eliminated with the newer derivation of thermal inertia [*Putzig and Mellon,* 2007b] and because thermal inertia from the TES database in the PDS is readily integrated with the TES-derived olivine contents from *Koeppen and Hamilton* [2008], all subsequent work described herein uses TES thermal inertia derived from the method of *Mellon et al.* [2000]. In selecting the TES data, we allowed thermal inertia quality flags of 0 (“best”) to 3 (“low”) to minimize the data density discontinuities.

3.2. TES Regional Analyses

We next examined three previously identified olivine-rich regions using TES data to determine if a positive correlation between thermal inertia and olivine abundance exists at a more regional scale (Table 1). The first region we examined surrounds the Nili Fossae, where *Bandfield et al.* [2011] previously found a qualitative positive correlation between thermal inertia and olivine abundance using THEMIS imagery. To examine this correlation using TES-derived olivine abundances at multiple scales, we defined three regions of interest (ROIs) in the area (Figure 2) and examined TES data within each region that met our selection criteria. The large ROI (black box in Figure 2) covers a large portion of the olivine-bearing Nili Fossae, whereas the medium ROI (solid while box) is limited to the northeast portion where the strongest olivine signatures (as indicated by purplish color in the DCS mosaic) are located. The small ROI (white dashed box) covers approximately the area of the THEMIS images used by *Bandfteld et al.* [2011]. The density cloud plots for the all three ROIs indicate that for all olivine abundances (0–70%) there exist a wide range of thermal inertias (0–600J m^{-2} K^{-1} $s^{-1/2}$) and a particular relationship between thermal inertia and olivine abundance is not apparent. However, when we plot the average normalized olivine abundance of each thermal inertia bin, both the large and small ROIs show a generally positive correlation between thermal inertia and average olivine abundance (Figure 3). The large ROI also displays evidence of a nonlinear correlation. The medium ROI, however, does not display a simple positive relationship between thermal inertia and olivine abundance and instead suggests a more complex relationship between the two variables.

The southern rim of the Isidis basin also has been identified previously as a region where the highest thermal inertia areas appear to be the most olivine enriched on the basis of THEMIS imagery [*Bandfield et al,* 2011]. We delineated three ROIs in this area based on the distribution of olivine-rich exposures suggested by 8–7-5 DCS daytime THEMIS images (Figure 4). The large ROI encompasses roughly the entire olivine-bearing region in southern Isidis, whereas the medium ROI covers only the two largest olivine-bearing exposures to the east. The small ROI is approximately the area covered by the THEMIS images analyzed by *Bandfield et al.* [2011]. The normalized olivine abundance and apparent thermal inertia for all observations are shown in Figure 5. As for Nili Fossae, there is a large range of thermal inertias (~100–700J m^{-2} K^{-1} $s^{-1/2}$) for nearly all olivine abundances (0–60%). The average olivine abundance of all thermal inertia bins in each of these ROIs is also shown in Figure 5. For all three ROIs, there is a generally positive correlation between thermal inertia and olivine abundance suggesting that the surfaces dominated by the smallest particle sizes do indeed have the lowest olivine abundances in the area.

Another region that has significant, but more spatially limited, olivine-bearing signatures is Argyre Planitia [*Bandfield and Rogers,* 2008; *Koeppen and Hamilton,* 2008]. This region shows spectral evidence from 8–7-5 DCS THEMIS images for olivine over a fairly large region (~670,000 km^2), but individual exposures of olivine are smaller and less distinct than in the other examined regions (Figure 6). The normalized olivine abundances (0–90%) do show a large spread in thermal inertia (0–580J m^{-2} K^{-1} $s^{-1/2}$), but in this case the highest olivine abundances (>40%) generally have more limited thermal inertias (100–430J m^{-2} K^{-1} $s^{-1/2}$) (Figure 6b). The binned data show that the relationship between TES-derived thermal inertia and olivine abundance is complex and confirm a peak in olivine abundance at low to moderate thermal inertia ~188–235 J m^{-2} K^{-1} $s^{-1/2}$ (value range represents thermal inertia range of a single bin; this notation is used hereafter) (Figure 6c). Smaller ROIs within Argyre Planitia showed the same complex relationship between thermal inertia and olivine abundance, commonly with a peak in olivine abundance at lower thermal inertias (<300$Jm^{-2}K^{-1}$ $s^{-1/2}$).

3.3. Seasonal Variability of Apparent TES Thermal Inertia

Putzig and Mellon [2007b] investigated the seasonal variability of TES-derived apparent thermal inertia and concluded that observed variations resulted from the vertical and horizontal heterogeneities of the Martian surface materials below the TES footprint (~3 km) and within a seasonal thermal skin depth of the surface. Because we are combining TES observations over multiple seasons to define and group the data into the thermal inertia bins, this may result in a single surface being included in multiple bins if its thermal inertia varies with season. To minimize this effect, we developed a method based on the work of *Putzig and Mellon* [2007b] to identify seasons where the regional apparent thermal inertia appears to be affected by heterogeneity and excluded TES observations during these periods. We used the analysis tools on the MarsTherm website (http://martherm.boulder.swri.edu [*Putzig et al.,* 2013]) to produce 10° L_S binned maps of the TES daytime thermal inertia for the Nili Fossae region (using the large ROI extents). We calculated the median thermal inertia of the map for each of these bins to represent the seasonal, regional thermal inertia and then calculated the median and one standard deviation of the seasonal values to define the

nominal daytime thermal inertia range of the Nili Fosse region (Figure 7). The median operator provides a better representation of the annual thermal inertia of the region as the seasonal thermal inertia departures can be large and nonlinear [*Putzig and Mellon,* 2007b]. As expected some excursions in median thermal inertia occur, particularly around $L_S = 60°$ −110° and $L_S = 160°$−180°. We discarded all TES observations that fell within these seasons, defined new thermal inertia bins based on the remaining data, and calculated the average olivine abundances for each bin. Plots for all three ROIs are shown in Figure 8. The density plots are generally unchanged from the all-data case (Figure 3) with all ROIs displaying a wide range of thermal inertias for nearly all olivine abundances, but some small changes are apparent. Both the large and medium ROIs have had all observations with olivine abundances over 60% removed, and the small ROI has a more limited range in thermal inertia (~150–350J m^{-2} K^{-1} $s^{-1/2}$) than in the all data case. However, the binned data illustrate that overall, the general relationship between thermal inertia and olivine abundance did not change. The large and small ROIs both show the same general relationship between thermal inertia and olivine abundance as the all-data case shown in Figure 3. The medium ROI does show a slightly modified relationship between thermal inertia and olivine abundance, notably a lowered olivine abundance in the lowest thermal inertia bins, but still shows a complex (nonpositive and nonlinear) correlation as the all-data case in Figure 3. In summary, we find that the relationships between thermal inertia and derived olivine abundance in the Nili Fossae region do not change significantly when accounting for the seasonal variance of TES thermal inertia, and so we do not investigate seasonal variations in thermal inertia for the other two TES regions (south Isidis and Argyre Planitia).

3.4. Local Analyses With THEMIS, CRISM, CTX, and HiRISE

THEMIS offers a substantial improvement in spatial resolution over TES (−100 m/pixel versus ~3 × 6 km/pixel) and allows us to consider whether the relationship between thermal inertia and derived olivine abundance changes if we examine even smaller areas. Before discussing the results for individual localities, it is important to note that the atmospheric correction algorithm of *Bandfield et al.* [2004] is fairly sensitive to the surface spectrum used and location specified for the training region. Depending on these two parameters during the atmospheric correction processing step, the distribution and magnitude of the resultant modeled end-members changed, sometimes significantly. In addition, relatively few THEMIS images cover an area that is spectrally homogenous, has a known composition, and is within −0.5 km elevation of the area of interest, which are all recommended conditions for the atmospheric correction algorithm [*Bandfield et al.,* 2004; *McDowell and Hamilton,* 2007]. We obtained the most consistent atmospheric corrections when we used a training region that appeared to be dust covered, so that we could use the TES- derived high-albedo (surface dust) shape to determine the atmospheric contribution to the scene (e.g., Isidis Planitia (Figure 9)) [*Bandfield and Smith,* 2003]. If a dusty area was not present within the image, a TES-derived spectrum of Surface Type I was used for an area that appeared spectrally basaltic [*Bandfield et al.,* 2000a] (e.g., Nili Fossae (Figure 11), Argyre Planitia (Figure 13), and Terra Cimmeria (Figure 17)). Using a well-characterized TES surface spectrum will generally result in less error as it reduces the dependence of the algorithm on the proper modeling of atmospheric and surface components of an unknown TES spectrum

(J. L. Bandfield, personal communication, 2014). This also allowed us to more directly compare our Isidis results to that of *Bandfield et al.* [2011] who also used the TES-derived high-albedo dust shape to atmospherically correct the same THEMIS daytime image (J. L. Bandfield, personal communication, 2014). For all cases we confirmed that the atmospheric correction produced reasonable results based on the expected distribution and spectral character (band shape and minima locations) of the resulting THEMIS surface spectral image. In summary, we limited our THEMIS image analyses to those where a dust-covered or Surface Type I (basaltic) surface within ~0.5 km elevation of the olivine-bearing area of interest could be found.

3.4.1. Southern Isidis—As a first step, we wanted to demonstrate that we could reproduce the end-member modeling results of *Bandfield et al.* [2011] using the same THEMIS image pair in southern Isidis. In doing so, we determined that those investigators applied a noise removal filter [*Edwards etal.,* 2011; J. L. Bandfield, personal communication, 2014] to the THEMIS daytime images prior to the atmospheric correction, which is generally not advised when using the images for quantitative analysis [*Edwards et al.,* 2011]. In addition, the same filter was not applied to the nighttime THEMIS images used to calculate thermal inertia and therefore could complicate the interpretation of any correlation between thermal inertia and derived olivine abundance (J. L. Bandfield, personal communication, 2014). To test the effects of using such a filter on the daytime THEMIS image only, we processed daytime THEMIS image I01395005 both with and without the noise removal step (all other processing exactly the same) and compared their correlations with unfiltered thermal inertia (Figure 9). The general spatial distribution of the modeled end-members (basalt, dust, and olivine-bearing material) is generally unchanged between the two cases, but in modeling the image that has had a noise removal filter applied, the modeled abundances are different, with a greater number of pixels in the image being modeled as a pure end-member (Figure 9a). If the nighttime image is density sliced by thermal inertia and the average olivine-bearing material abundance of these bins calculated using both the filtered and unfiltered images, there is a generally positive correlation between thermal inertia and olivine-bearing material abundance, although in both cases the relationship appears nonlinear. However, in the case when a noise removal filter is applied, the average olivine-bearing material abundances for the lower thermal inertia bins are lowered (Figure 9). We also processed a second daytime THEMIS image that covered the same area (I39907019; no noise removal filter applied) to rule out the effect of observational conditions on the relationship between derived olivine-bearing material abundance and thermal inertia and confirmed that a the same generally positive correlation existed despite the different imaging conditions (not shown).

Although TES and THEMIS data indicate a positive correlation between thermal inertia and olivine abundance, it is unclearat these spatial scales if all units within the area are geologically related from a weathering perspective. This is a required assumption if these data are intended to be used to deduce the chemical weathering behavior of olivine. Higher-resolution spectral data and imagery (Figure 10) do indeed suggest that not all units present within the THEMIS image (Figure 9) are geologically related. Figure 10a shows the CRISM olivine index from image FRT00007F47 over a portion of the southern Isidis olivine-bearing

unit in contact with the large plain of the Isidis basin floor (modeled as basalt and dust with THEMIS; Figure 9). The distribution and strength of the CRISM olivine spectral signature is consistent with the THEMIS modeling results and verifies that the olivine signature is much weaker in the plain unit. The contact between the plain unit and the olivine unit is sharp, and the plain unit appears to superpose the olivine-bearing unit (Figure 10b). At higher resolution it is evident that the plain unit stratigraphically overlies the olivine unit and is therefore not derived from the olivine unit (Figure 10c). This plain unit is most likely the partially dust-covered basaltic volcanic flow that covers the Isidis basin floor, including the olivine-bearing unit, which has been documented by other studies. [*Tornabene et al.,* 2008; *Bishop et al.,* 2013]. Small bright dunes are also present in the area, but the source of the sand is not clear and the strongest olivine signature according to CRISM is from the exposed underlying rock (Figure 10d). The other major olivine-poor unit in the area is a large bright-toned mound (Figure 10b), which is also not derived from the olivine unit and is more likely a high-standing massif of ancient, altered basalt basement rock which outcrops across the southern Isidis rim area [*Tornabene et al.,* 2008; *Bishop et al.,* 2013]. Because the major olivine-poor units within the southern Isidis rim are not weathering products of the olivine-bearing unit exposed here, the positive correlation between thermal inertia and olivine abundance, although strong, cannot be used to infer a chemical weathering history of olivine.

3.4.2. Nili Fossae—In the Nili Fossae region *Bandfield et al.* [2011] noted that the spatial relationship between olivine-rich and high thermal inertia surfaces was less clear than for the Isidis region. To investigate this in more detail, we analyzed the same image pair and again verified that although not recommended, applying a noise removal filter to daytime THEMIS data does not significantly alter the correlation results (from this point forward we only use data that have not had such a filter applied). Results for the unfiltered data are presented in Figure 11. The distribution and concentrations of basalt, high-silica, and olivine-bearing material generally match that of *Bandfield et al.* [2011] despite the absence of a noise filter applied to the daytime image. As noted by *Bandfield et al.* [2011], the spatial correlation between high thermal inertia and olivine-bearing surfaces is less clear than it is in Isidis. In particular, high thermal inertia surfaces in the southern portion of the image are partially modeled as olivine (purple in 8–7-5 DCS) and as high silica (pink to orange-red in 8–7-5 DCS). Regardless, there is a generally positive, nonlinear correlation between thermal inertia and the abundance of olivine-bearing material in the scene overall (Figure 11b).

Despite the positive correlation suggested by THEMIS data, the complicated spatial relationship of thermal inertia and olivine signatures warranted investigation of the area in more detail. We examined several CRISM olivine index images that intersected the THEMIS daytime image and found that the strength of the index was consistent with THEMIS modeling results (Figure 12a). HiRISE imagery of the area revealed that the olivine-bearing unit stratigraphically overlies the relatively olivine-poor, bright-toned unit that has a coherent, massive appearance (i.e., not loose sediment although it is partially covered by some; Figure 12b). The stratigraphic position and massive appearance of the olivine-poor unit strongly suggests that it is not a direct weathering product of the olivine-rich unit that lies above it. This interpretation is supported by other work that has mapped the olivine-poor

bright-toned unit as altered basement rock stratigraphically underlying the olivine-bearing unit [*Ehlmann et al.,* 2009; *Mustard et al.*, 2009]. Further, these workers showed that this olivine- poor altered basement unit outcrops throughout the Nili Fossae region and often in proximity to the olivine-rich unit. This clearly demonstrates that we cannot assume that all relatively olivine-depleted material in the THEMIS daytime image, or even in the larger Nili Fossae region examined by TES, is a direct weathering product of the olivine-rich unit. This failed assumption prevents the apparent relationship between thermal inertia and olivine abundance to be used to infer the chemical weathering of olivine, despite the strong positive correlation between the two variables indicated by both instruments.

However,the presence of olivine-bearing dunes evident in Figure 12 is intriguing as this might be evidence of sediment directly derived from the more massive olivine-bearing material topographically above it. Although these dunes are not resolvable in the THEMIS data, the CRISM olivine index suggests that they are olivine-poor but olivine-bearing (green/yellow) relative to the olivine-rich unit (red/orange). These olivine-bearing sands are present throughout the Nili Fossae region [*Hamilton and Christensen*, 2005; *Mustard et al.*, 2009; *Edwards and Ehlmann,* 2015; *Goudge et al.,* 2015] and are also interpreted by other workers to derive from the olivine-rich unit in Nili Fossae [*Mustard et al.*, 2009; *Edwards and Ehlmann,* 2015]. However, modeling of CRISM data by *Edwards and Ehlmann* [2015] of the olivine-bearing sands and olivine-bearing unit indicates that their respective olivine abundances are indistinguishable. They model the sand as 65% basalt, 25% olivine, and 8% carbonate and the olivine-bearing unit as 59–70% basalt, 24–26% olivine, and 1–15% carbonate (the olivine-bearing unit is partially altered to carbonate in lower stratigraphic sections [*Ehlmann etal.,* 2008]). If the sand is indeed derived from the olivine-bearing unit, this implies that significant chemical weathering of olivine did not occur as sediment mechanically weathered out of the rock.

3.4.3. Argyre Planitia—In Argyre Planitia TES data indicate that thermal inertia and olivine abundance are not positively correlated as the peak olivine abundance occurs at lower thermal inertias (~188–235 J m^{-2} K^{-1} $s^{-1/2}$) (Figure 6). To investigate this result at higher spatial resolution, we selected a THEMIS image pair in the northwest corner of the region that covered an area with a relatively strong olivine signature according to 8–7-5 DCS THEMIS imagery (Figures 6 and 13). Using the full area of overlap between the day (olivine) and night (thermal inertia) images, we see a nonlinear but generally positive relationship between thermal inertia and the abundance of olivine-bearing material (Figure 13b). However, most of the olivine-bearing surfaces are limited to the southern portion of the THEMIS image and are not associated with high thermal inertias. The small solid white boxes in Figure 13a highlight one location with a high abundance of THEMIS-derived olivine-bearing material (85%;average within box) and a moderate thermal inertia (318J m^{-2} K^{-1} $s^{-1/2}$;aver-age within box). But the moderate thermal inertia bin (~300–376J m^{-2} K^{-1} $s^{-1/2}$) in the THEMIS data plot (Figure 13b) has an average olivine-bearing material abundance of only ~43%. This large discrepancy is likely the result of the moderate thermal inertia bin including surfaces with low olivine abundance, i.e., the large dusty plain to the north of the olivine-bearing region (Figure 13a). Inclusion of this surface is suitable for our analysis if this plain is a direct weathering product of the olivine-rich hills to the south, but

as we showed in the case of both Isidis and Nili Fossae geological relationships cannot always be assumed at the scale of THEMIS.

Higher-resolution CTX imagery does strongly indicate that the large dusty plain north of the olivine-bearing hills is geologically unrelated to the olivine-rich unit (Figure 14). The plain itself is bright toned with a nearly smooth surface with subtle texture at the highest resolution of the CTX image (5.1 m/ pixel). The contact of the dusty plain with surrounding mounds is sharp with significant relief and is visible in several areas around and up to the mounds. Based on its coherent nature, relatively smooth texture, and geomorphological expression, we interpret the plain unit as a lava flow that has embayed the surrounding higher topography. Therefore, this unit is not a weathering product of the olivine-bearing hills and the northern plain area should not be included in the correlation analysis.

Accordingly, we next limited the analysis to only the olivine-bearing hills and directly surrounding areas within the THEMIS images (dashed white lines in Figure 13a). As expected, the moderate thermal inertia bin (~300– 376 J m^{-2} K^{-1} $s^{-1/2}$) now displays the highest abundance of olivine-bearing material (65%), whereas the higher thermal inertia bins have less (~56–60%) (Figure 13c) and it is immediately apparent that there is complex, non-correlated relationship between thermal inertia and olivine-bearing material abundance in even this limited area (Figure 13c). Further, CTX imagery again suggests that not all units are geologically related. Figure 14c shows an outcropping bright-toned, textured mound in the middle of the valley that is obviously not a weathering product of the nearby olivine-bearing hills but is more likely an exposed underlying stratigraphic unit. Loose sediment and dunes do surround the mound, but it is difficult to tell at THEMIS resolution which areas of the valley floor have the strongest olivine signature, although THEMIS data indicate that the valley is olivine poor relative to the hills (Figure 13a) which has been found elsewhere in Argyre [*Bandfield and Rogers,* 2008; *Buczkowski et al.,* 2008]. Unfortunately, at the time of writing, publicly accessible targeted CRISM images covering this area do not have IR detector data, which have proven most useful for the definitive detection of olivine [e.g., *Pelkey et al.,* 2007; *Salvatore et al.,* 2010; *Viviano-Beck et al.,* 2014]. Regardless, geomorphologic features visible at higher spatial resolution than that permitted by THEMIS again suggest that not all surfaces within even this limited area are geologically related from a weathering perspective, complicating the use of the relationship between thermal inertia and olivine-bearing material abundance to determine olivine weathering trends in Argyre Planitia as well.

3.5. Areas of Low Thermal Inertia and High Olivine Abundance

Although the olivine-bearing units in southern Isidis and Nili Fossae generally have the highest thermal inertia in the region consistent with previous studies [*Hamilton and Christensen,* 2005; *Bandfield et al.,* 2011], in Argyre Planitia we find that the olivine-rich units are not coincident with the highest thermal inertia in the area and are instead associated with low to moderate thermal inertias (~300–376J $m^{-2}K^{-1}$ $s^{-1/2}$; THEMIS). This contrasts with a previous study that suggested that olivine-bearing materials are generally limited to “high” (value not specified) thermal inertia surfaces [*Bandfield etal.,* 2011]. In an effort to identify additional olivine-rich areas with low to moderate thermal inertia, we searched for

lower thermal inertia areas with relatively high olivine abundances with TES. Specifically, we isolated TES observations where the derived olivine abundance is greater than 25% and the TES daytime thermal inertia (of the same observation) is less than 350 J m^{-2} K^{-1} $s^{-1/2}$. We created a map of these observations binned at 2° per pixel to locate the 12 bins (eight locations) with the highest number of detections shown in Figure 15. We then examined TES data along with THEMIS 8–7-5 DCS imagery at each location. Two locations (red squares in Figure 15) are likely spurious detections of olivine because they represent an along-track detection of olivine in one TES orbit with an absence of comparable olivine detections in other colocated orbits. Three locations (yellow squares in Figure 15) represent ambiguous detections. In these areas some olivine appears to be present in the area (on the basis of valid TES detections and 8–7-5 DCS THEMIS imagery) but we could not clearly identify low thermal inertia/high olivine abundance materials at the TES or THEMIS scale.

Two locations (blue squares in Figure 15) represent dust-covered and olivine-rich surfaces areally mixed at the TES scale. One detection lies on the eastern edge of the olivine-rich Nili Fossae and shows elevated olivine abundances for the lowest thermal inertia bins at the TES scale (not shown). However, directly to the west of this detection is an area that contains a significant amount of dust cover, as evidenced by its elevated dust cover index (Figure 15) [*Ruff and Christensen,* 2002]. In addition, optically thick (at thermal infrared wave-lengths) dust in the Nili Fossae region has been noted by other workers [*Hamilton and Christensen,* 2005]. Therefore, we examined this area with higher-resolution THEMIS data (images I36251026 and I09578012; not shown). As expected, a significant amount of dust was modeled within the image along with olivine-enriched areas with relatively higher thermal inertia. Therefore, the relatively large TES pixels (−3×6 km) are covering both olivine-rich surfaces and dusty, low thermal inertia surfaces, leading to the TES observation that low thermal inertia surfaces have a high olivine abundance. Our investigation of the other high olivine abundance/low thermal inertia that lies on border between Herschel crater and a large dusty region to the north (other blue square in Figure 15) suggests that this detection is also the result of TES areally mixing dusty and olivine-bearing surfaces. These two locations illustrate how the relationship between thermal inertia and olivine abundance can change significantly depending on the scale of observation (TES versus THEMIS).

The last location, located within Terra Cimmeria (green square in Figure 15), is a valid detection of a low thermal inertia unit (~272$Jm^{-2}K^{-1}$ $s^{-1/2}$; TES derived) with a significant abundance of olivine (16%; TES derived) (Figures 16and 17). Based on THEMIS 8–7-5 DCS imagery and TES nighttime thermal inertia, it appears that large craters in the area are excavating olivine-bearing material from beneath a higher thermal inertia unit (Figure 16). Both TES ROIs drawn in the area have a range of thermal inertias for most olivine abundances, but the binned data suggest that the highest thermal inertia units are not the most olivine bearing (Figures 16c and 16d) and that the highest olivine abundance is associated with a unit having a thermal inertia of around 290– 310$Jm^{-2}K^{-1}$ $s^{-1/2}$ (Figures 16e and 16f). End-member modeling of THEMIS daytime image I08440010 confirms the higher abundance of olivine-bearing material of the crater ejecta relative to the higher thermal inertia plains and also confirms that dust abundance in the area is low (Figure 17a). Although the THEMIS data seem to confirm that the highest olivine-bearing material abundance is associated with an intermediate thermal inertia bin (262–328J m^{-2} K^{-1} $s^{-1/2}$),

we note that the highest thermal inertia bin (328–410J m^{-2} K^{-1} $s^{-1/2}$) has a modeled olivine-bearing material abundance (44%) that is not statistically separable from that of the lower bin (45%). The distribution of compositions for this image appears somewhat noisy, with the vast majority of the image being modeled as basalt with small amounts of dust and olivine in some areas (Figure 17a). We suspect that the low surface temperatures within the image (maximum brightness temperature 256 K) is causing relatively low signal-to-noise and reduced spectral contrast among the bands, making it more difficult for the modeling algorithm to differentiate areas of different spectral character. Therefore, we examined TES pixels around one of the larger craters in more detail to confirm the modeled olivine differences between the crater ejecta and plains material (Figure 17c). As measured by TES, the crater ejecta unit does have both a lower average thermal inertia (272 J m^{-2} K^{-1} $s^{-1/2}$) and higher average olivine abundance (16%) compared to the plain unit (352 J m^{-2} K^{-1} $s^{-1/2}$ and 7%), confirming that in this area relatively low thermal inertia materials are characterized by olivine abundances that are significantly higher (16%) than that of higher inertia materials (7%).

4. Discussion

4.1. The Relationship Between Olivine Abundance and Thermal Inertia

We find that materials on Mars having TES-derived olivine abundances above the detection limit of ~5% [*Koeppen and Hamilton,* 2008] exhibit a wide variety of thermal inertias (Figure 1 and Table 1). Although *Koeppen and Hamilton* [2008] found that olivine abundances of up to 10–20% are common in the southern highlands, we find that globally, the most typical olivine abundance is ~5–7%, consistent with the calculated 5.1% average olivine abundance (for surfaces within ±60° in latitude, mean standard error of olivine abundance 2.4%) found by *Rogers and Hamilton* [2015]. Further, out of the 10 mineral classes (i.e., compositional provinces) on Mars defined by *Rogers and Hamilton* [2015], only one province (class 10; Nili Fossae) was found to have an average olivine abundance above 10% (at 11 ± 5%). Therefore, our findings confirm earlier work with TES that the most typical olivine abundance on Mars is ~5–7% and establishes that these typical olivine abundances are found at a wide variety of apparent thermal inertia values, dominantly at 100–400 J m^{-2} K^{-1} $s^{-1/2}$ but commonly at 25–600 J m^{-2} K^{-1} $s^{-1/2}$ (Figure 1). Further, we find that even higher olivine abundances (up to ~25%) display a similarly large spread in spatially correlated thermal inertia at the TES scale and that the majority of high olivine abundance (>25%) materials have a thermal inertia less than 400J m^{-2} K^{-1} $s^{-1/2}$ (Figure 1). This contrasts with the results of *Bandfteld et al.* [2011] who suggested that olivine-bearing surfaces are usually associated with high (value not specified) thermal inertia surfaces.

At a global scale there is no apparent correlation between olivine abundance and thermal inertia, which is unsurprising given that our key assumptions likely fail at the global scale (for example, the assumption that all lower inertia materials are directly derived from the higher inertia materials in the data set). Examining the data at smaller spatial scales, two of the largest olivine-bearing regions, Nili Fossae and Isidis, show evidence from TES and THEMIS that thermal inertia and olivine abundance are positively correlated, suggesting that chemical weathering of olivine-rich rock is a plausible explanation for olivine-depleted

sediments in these areas [*Bandfteld and Rogers,* 2008; *Bandfteld et al.,* 2011]. However, observations of the geological relationships of units within both of these areas reveal that not all olivine-poor surfaces represent weathering products of the olivine-rich units. The implications of this are explored in more detail in section 4.2 below.

For two other olivine-bearing regions, Terra Cimmeria and Argyre Planitia, we find that a simple, positive relationship between thermal inertia and olivine abundance does not exist and that there are significant (i.e., detectable at the spatial scale of TES) deposits of low thermal inertia (188–272 J m^{-2} K^{-1} $s^{-1/2}$; TES derived), olivine-rich material (16%; TES derived). In Terra Cimmeria, relatively low thermal inertia (272 J m^{-2} K^{-1} $s^{-1/2}$) crater ejecta overlie a higher thermal inertia plain unit (352 J m^{-2} K^{-1} $s^{-1/2}$). The low thermal inertia material retains a significant olivine abundance (16%; TES derived), whereas the plain unit olivine abundance is that of a typical Martian surface (7%; TES derived). Although the geologic setting and stratigraphic relationship of the two units strongly suggest that the crater ejecta unit is not a direct weathering product of the plain unit, it is compelling that the crater ejecta has a significant olivine abundance despite an apparent thermal inertia most consistent with sand [*Presley and Christensen,* 1997; *Fenton et al.,* 2003]. Furthermore, a separate study using OMEGA data noted that small crater ejecta with olivine spectral signatures are common in Terra Cimmeria, suggesting that more sand-sized, olivine-bearing materials may be present in the area below the spatial resolution of TES [*Odyetal.,* 2012]. Similarly in Argyre Planitia, it is significant that low thermal inertia materials (188–235 J m^{-2} K^{-1} $s^{-1/2}$; TES derived) consistent with sand-size particles exhibit such a significant abundance of olivine (16%; TES derived) (Figure 6). We note that a high olivine abundance in sand could occur via enrichment by segregation of olivine from a relatively olivine-poor source during aeolian processing such as has been documented on Earth and proposed for Mars [*Mangold et al.,* 2011]. However, there is no evidence for this process, such as olivine-enriched dune forms, at either location at the scale of the available data. Regardless, material with an apparent particle size of sand and significant olivine abundance suggests that chemical weathering of olivine from the original bedrock source has been limited in these areas.

It is possible that the ~16% olivine abundance of apparently sand-dominated units is the result of the chemical weathering of an even more olivine-rich parent unit that is either no longer present (e.g., Argyre Planitia) or buried (e.g., Cimmeria Terra). Although we cannot rule out the (prior) existence of such units or know how much olivine they contained, we can compare the olivine abundance of the sandy materials to materials with a similar thermal inertia in other olivine-enriched regions. For Nili Fossae, materials with TES thermal inertias of 250–323 J m^{-2} K^{-1} $s^{-1/2}$ have average TES-derived olivine abundances of 11–13% (ignoring the medium ROI that covers only the eastern portion of Nili Fossae and therefore may be influenced by the dust cover that complicates TES observations in this area (Figure 15)). For southern Isidis and Argyre Planitia all thermal inertia surfaces 300J m^{-2} K^{-1} $s^{-1/2}$ or less have a maximum TES-derived olivine abundance of 10%. So 16% olivine for a 188–272 J m^{-2} K^{-1} $s^{-1/2}$ material is higher (>3–6%) than all other olivine-bearing units having similar thermal inertias and significantly higher (>6%) than all locations but one (Nili Fossae). Therefore, a 16% olivine abundance is much higher than either the typical Martian surface (5–7%) or moderate (~300J m^{-2} K^{-1} $s^{-1/2}$) thermal inertia materials derived from

other olivine-rich, rocky regions on Mars. This observation, combined with the lack of an obvious nearby source (a higher thermal inertia and higher olivine abundance unit), suggests that these high olivine abundance, sand-sized materials may not be easily explained as chemical weathering of rock even richer in olivine to produce relatively olivine-poor sediments.

Numerous other studies have similarly reported smaller-scale olivine-bearing sand deposits on Mars. Several of the olivine-bearing Amazonis Planitia intracrater deposits described by *Stockstill-Cahill et al.* [2008] display prominent dune forms indicating that the olivine-bearing material is likely composed of sand-sized particles although those investigators did not quantify the thermal inertia of individual deposits. *Schneider and Hamilton* [2006] did report apparent TES thermal inertia ($370 Jm^{-2}K^{-1} s^{-1/2}$) for an olivine-bearing (15%; TES-derived) intracrater Amazonis Planitia deposit but noted that it likely represented a mixture of the rock and sand that comprised the deposit. *Tirsch et al.* [2011] surveyed dark sands within 70 Martian craters on a global scale and have found evidence for the presence of olivine within 30% of them using OMEGA. They concluded that the presence of olivine in sediment eroding out of layers within the craters indicated little chemical weathering of olivine during sediment production [*Tirsch et al.,* 2011]. *Chojnacki et al.* [2014a] also surveyed dune fields on a global scale and detected olivine with CRISM in 56% of characterized dunes ($n = 60$) within Valles Marineris (VM) and 46% of those outside VM ($n = 30$). In the companion study *Chojnacki et al.* [2014b] detailed the VM dunes including their sources and concluded that several olivine- bearing dunes and sources have very similar CRISM spectra indicating preservation of the olivine and little chemical weathering. This is similar to the Nili Fossae where sand and source rock were found to have indistinguishable olivine abundances with CRISM [*Edwards and Ehlmann,* 2015]. However, both *Tirsch etal.* [2011] and *Chojnacki et al.* [2014b] noted that in some cases olivine appeared less abundant in dune sands further from their source. Although these observations were attributed to aeolian segregation [*Chojnacki et al.,* 2014b] and olivine detection issues for small particle sizes in the VNIR [*Tirsch etal.,* 2011], it is plausible that these trends also could be explained via chemical weathering of olivine. Regardless, this apparent commonality of olivine-bearing sands on Mars warrants more investigation as it implies that the derived sediment has retained olivine despite obvious mechanical weathering (in addition to possible chemical weathering) from its source rock.

In summary, the emerging picture is that olivine-bearing materials on Mars exhibit a wide range of apparent thermal inertias and therefore a variety of effective particle sizes. This is consistent with a global olivine study using OMEGA spectral maps that also found a wide range of TES thermal inertias (~100 to 600 $J m^{-2} K^{-1} s^{-1/2}$, with a peak around 225 $J m^{-2} K^{-1} s^{-1/2}$) associated with OMEGA olivine detections [*Odyetal.,* 2013]. We note that TES olivine detections have a similar spread of apparent TES thermal inertias (Figure 1). In addition, two regions (Argyre and Terra Cimmeria) contain significant deposits of olivine-enriched materials with a thermal inertia consistent with sand and other studies have documented numerous smaller-scale deposits of olivine-bearing sands elsewhere on Mars [*Schneider and Hamilton,* 2006; *Stockstill-Cahill et al.,* 2008; *Tirsch et al.,* 2011; *Chojnacki et al.,* 2014a, 2014b; *Edwards and Ehlmann,* 2015]. While the lack of a unambiguous source material precludes the use of these data to infer the chemical weathering history of olivine,

the present and previous studies suggest that there are significant deposits of olivine-bearing material with low to moderate thermal inertia (<400J m^{-2} K^{-1} $s^{-1/2}$) and that not all olivine-rich materials exhibit high thermal inertia [e.g., *Bandfield et al.,* 2011].

4.2. Evidence for Chemical Alteration of Olivine

The primary goal of our study is to examine the relationship between olivine abundance and thermal inertia to investigate whether it can be used to infer the chemical weathering of olivine in the process of mechanical weathering on Mars. Inherent in this analysis is the assumption that the olivine-rich and olivine-poor materials have a genetic relationship; however, we find in all four of our study regions (Nili Fossae, southern Isidis, Argyre Planitia, and Terra Cimmeria) that this is not the case. Specifically, we find in every case that when the detailed geomorphology and stratigraphic relationships of the units are considered, this key assumption fails and therefore no conclusion can be drawn regarding the degree of chemical alteration of olivine that has occurred.

Two regions, Nili Fossae and southern Isidis, exhibit a generally positive correlation between thermal inertia and olivine abundance at the both the TES and THEMIS scales. However, we find that despite the chemical weathering trend suggested by these relationships, local geomorphological analysis with higher-resolution CRISM data and HiRISE imagery reveals that the local geology is complex with several units that are unrelated from a weathering perspective. Therefore, not all of the relatively olivine-poor sediment are direct weathering products of nearby olivine-rich, high thermal inertia surfaces, and a generally positive correlation between thermal inertia and olivine abundance cannot be used in either area to infer an olivine chemical weathering history. This is in contrast to the conclusions of *Bandfield etal.* [2011] for both areas, who interpreted the generally positive correlation between olivine abundance and thermal inertia as evidence of chemical weathering. Although they used higher-resolution imagery to verify that olivine-bearing materials have a more coherent, rocky appearance compared to nearby olivine-poor materials, they did not elaborate on the geological relationship between the two groups of materials. Our analysis shows that their stratigraphic relationships are inconsistent with the lower inertia, higher olivine abundance materials being derived from the higher inertia, lower olivine abundance materials.

In Argyre and Terra Cimmeria, although the relationship between olivine abundance and thermal inertia is shown to be more complex, we find that even the materials in the area with the greatest olivine abundances have no direct weathering relationship to materials with lower olivine abundance. In Argyre there are both lower and higher thermal inertia materials with a lower olivine abundance (Figures 6b and 13c), and geomor-phologic analysis reveals that both materials are unrelated (from a stratigraphic and weathering perspective) to the olivine-enriched materials (Figure 14). In Terra Cimmeria olivine-enriched (16%; TES-derived) crater ejecta with a TES thermal inertia consistent with sand (272$Jm^{-2}K^{-1}$ $s^{-1/2}$) overlies relatively olivine-poor, higher thermal inertia plains materials. Although the crater ejecta have a higher olivine abundance than the underlying plains, we cannot use these data to infer an olivine weathering trend as they likely represent different units and/or have different weathering histories. For example, the two units may be separate units that are

geologically unrelated, or ejecta could represent material from the plain unit that was buried and therefore not exposed or weathered as much as the surface. Indeed, THEMIS data do suggest that there is an olivine-bearing (according to 8–7-5 DCS imagery) unit with THEMIS thermal inertia similar to the plain unit that outcrops several kilometers to the east but we could not determine with certainty the geologic or strati-graphic relationship of this unit to the crater ejecta and plain unit.

The olivine-bearing exposures in Argyre Planitia were also examined by *Bandfield and Rogers* [2008]. Using THEMIS imagery, they found that rockier (higher thermal inertia surfaces, ~550J m^{-2} K^{-1} $s^{-1/2}$) had a spectral absorption at longer wavelengths (10–12 μm, ~1000–830cm^{-1}) that they attributed to olivine. Those investigators stated that the pattern of higher inertia (rockier) surfaces having a more mafic-rich signature consistent with olivine relative to lower inertia units is common in Argyre Planitia. However, we have found that this pattern does not apply to all olivine-bearing areas in Argyre Planitia. Specifically, we have found an area where the highest thermal inertia surfaces (~470–588J m^{-2} K^{-1} $s^{-1/2}$) are not the most olivine enriched compared to lower inertia surfaces (~301–376J m^{-2} K^{-1} $s^{-1/2}$) as determined by THEMIS (Figure 13). This is further supported at a regional scale with TES, where the highest thermal inertia surfaces (458–573 J m^{-2} K^{-1} $s^{-1/2}$) have a significantly lower TES-derived olivine abundance (9%) than lower thermal inertia materials (188–235 J m^{-2} K^{-1} $s^{-1/2}$; 16% TES derived) (Figure 6). Although it is certainly possible (even likely) that the olivine-bearing materials found with THEMIS in this work and *Bandfield and Rogers* [2008] have different origins and weathering histories, it is worth noting that a significantly different olivine abundance/thermal inertia relationship was found in the same region ~250 km away. Thus, the geologic history of olivine-bearing units within Argyre Planitia appears to be complex and it is unsuitable to assume that because one small area displays evidence for chemical weathering of olivine, the rest of Argyre does as well. Therefore, when evidence of local chemical dissolution of olivine is found, caution should be used in attempting to draw inferences about larger regional- or global-scale olivine weathering processes.

4.3. Weathering Rinds and Rates

The evidence for weathering products on Mars has caused *McSween et al.* [2009] to question the derived mineralogy of surfaces from TES as a result of the presence of secondary (weathering) coatings that might complicate TIR spectral observations, which have a penetration depth on the order of tens to hundreds of microns. Indeed, several laboratory studies have investigated and verified that the presence of weathering rinds on basaltic particles tends to overestimate the proportion of secondary weathering products and underestimate the amount of primary igneous components due to the coating geometry of the weathering rind, which can lead to nonlinear spectral mixing [*Kraft et al.,* 2003; *Michalski et al.,* 2006; *Rampe et al.,* 2013].

Because this is a documented effect in the laboratory, it is prudent to consider how it might influence our observations and results with TES and THEMIS. The most basic interpretation is that if chemical alteration of olivine is taking place and therefore weathering products are being produced, this effect will lead to an underestimation of olivine abundance for such

materials. However, because we are interested in the correlation of olivine abundance with thermal inertia (as a proxy for particle size), if this effect is operating equally across all particle size ranges, it will not greatly influence our interpretations. If, however, the nonlinear spectral mixing effect is more pronounced for smaller particle sizes (due to greater amount of weathering and thus thicker rinds, for example), this would lead to a greater amount of olivine abundance underestimation as particle size decreases. Further complicating this nonlinear spectral effect of the weathering rind itself is the possible nonlinearity in the production of the weathering rind with respect to particle size. Although the weathering rate is generally expected to increase with decreasing particle size [e.g., *Lasaga,* 1984], there is evidence that the olivine weathering rate may decline as particle size decreases due to increased weathering rind thickness that increasingly "passivates" the underlying olivine surface [e.g., *Davaletal.,* 2010,2011].

This complex interplay of weathering rate, weathering rind production, and particle size is not well understood. Unfortunately, we are not aware of any studies that investigate weathering rind effects combined with particle size differences on TIR spectra, but we hypothesize that there could be an apparent nonlinear relationship between olivine abundance and particle size (thermal inertia) due to these effects. In particular, we note that several areas display nonlinear relationships between olivine abundance and thermal inertia. Although this is most likely due to the complicated geological relationships between units discussed above that prevent the interpretation of chemical weathering trends, it is possible that these relationships may also be influenced by complications from secondary weathering rinds. More work is needed to further investigate this possibility.

5. Conclusions

We have investigated, at a variety of spatial scales, whether the relationship between olivine abundance and thermal inertia on Mars, in the absence of other geologic information, is sufficient to infer chemical alteration of olivine-bearing surface materials. We find with global analysis of TES data that the most typical olivine abundance on Mars is ~5–7% and that olivine-bearing materials (5–25%) have a wide range of apparent thermal inertia values, commonly 25–600 J m^{-2} K^{-1} $s^{-1/2}$. TES also reveals that the majority of high olivine abundance (>25%) materials have an apparent TES thermal inertia less than 400 J m^{-2} K^{-1} $s^{-1/2}$. We find that for some olivine-enriched areas on Mars (southern Isidis and Nili Fossae) TES and THEMIS analysis does indicate that there is a positive correlation between thermal inertia and olivine abundance, which may be inferred as indicating that chemical alteration of olivine is resulting in the production of relatively olivine-poor sediment. However, within both of these regions, we have demonstrated with detailed investigation of local geology why such an inference may not be correct. Specifically, higher-resolution geomorphological analysis of these areas reveals that not all of the units present within the area have a direct weathering relationship to each other. We have identified two notable deposits (Argyre Planitia and Terra Cimmeria) with a significant olivine abundance (16%; TES-derived) and a thermal inertia consistent with sand-sized particles, although the lack of a nearby olivine-rich parent unit precludes the use of these observations to infer chemical weathering of olivine as well. In summary, we conclude that although some locations may exhibit a positive correlation between thermal inertia and olivine abundance, local geology and

stratigraphic relationships reveal that such correlations may not be causal and cannot be used to infer chemical weathering of olivine in any of the four areas examined in this study. More generally, olivine-bearing deposits on Mars have a wide range of thermal inertias (i.e., effective particle sizes) and are not primarily associated with high thermal inertia surfaces. These new findings do not preclude the chemical weathering of olivine in the process of sediment production on Mars, but they underline the need for detailed analysis and caution when extrapolating the interpretations of a few localities to a large, global-scale process.

Acknowledgments

Our sincere gratitude goes to Josh Bandfield and Deanne Rogers for sharing data and enlightening and useful discussions regarding this project and their earlier work related to it. Many thanks is also due to Hugh Kieffer and Eddy Barratt for their help in investigating the TES thermal inertia interpolation issue and for Eddy Barratt's work on the MarsTherm website (https://marstherm.boulder.swri.edu). Thanks to Robin Fergason for helpful discussions regarding THEMIS thermal inertia; to Tim Goudge for help with CRISM data and Nili Fossae geology; and to Kim Murray, Chris Edwards, Sadaat Anwar, and Ken Rios for invaluable technical help regarding ISIS, Davinci, and JMARS. We are grateful to Chris Edwards and an anonymous reviewer for their detailed and constructive reviews that helped to significantly improve the manuscript. Several figures in this paper were generated with the excellent JMARS software program [*Christensen et al.,* 2010]. This work was funded by a grant to V.E.H. from the Mars Data Analysis Program (NNX11A183G). All data used in this work are available from the NASA Planetary Data System (http://pds.nasa.gov) or from the MarsTherm website (https://marstherm.boulder.swri.edu).

References

Bandfield JL (2002), Global mineral distributions on Mars, J. Geophys. Res, 107(E6), 5042, doi: 10.1029/2001JE001510.

Bandfield JL, and Rogers AD (2008), Olivine dissolution by acidic fluids in Argyre Planitia, Mars: Evidence for a widespread process?, Geology, 36(7), 579–582.

Bandfield JL, and Smith MD (2003), Multiple emission angle surface-atmosphere separations of Thermal Emission Spectrometer data, Icarus, 161(1), 47–65.

Bandfield JL, Hamilton VE, and Christensen PR (2000a), A global view of Martian surface compositions from MGS-TES, Science, 287(5458), 1626–1630.

Bandfield JL, Christensen PR, and Smith MD (2000b), Spectral data set factor analysis and end-member recovery: Application to analysis of Martian atmospheric particulates, J. Geophys. Res, 105, 9573–9587, doi:10.1029/1999JE001094.

Bandfield JL, Rogers D, Smith MD, and Christensen PR (2004), Atmospheric correction and surface spectral unit mapping using Thermal Emission Imaging System data, J. Geophys. Res, 109, E10008, doi:10.1029/2004JE002289.

Bandfield JL, Rogers AD, and Edwards C (2011), The role of aqueous alteration in the formation of Martian soil, Icarus, 211, 157–171.

Bibring J-P, et al. (2005), Mars surface diversity as revealed by the OMEGA/Mars Express observations, Science, 307,1576–1581. [PubMed: 15718430]

Bishop JL, et al. (2013), Mineralogy and morphology of geologic units at Libya Montes, Mars: Ancient aqueously derived outcrops, mafic flows, fluvial features, and impacts, J. Geophys. Res. Planets, 118, 487–513, doi:10.1029/2012JE004151.

Bristow TF, et al. (2015), The origin and implications of clay minerals from Yellowknife Bay, Gale crater, Mars, Am. Mineral, 100(4), 824–836. [PubMed: 28798492]

Buczkowski DL, Murchie SL, Seelos FP, Malaret E, Hash CD, and the CRISM Science Team (2008), CRISM analysis of Argyre Basin, paper presented at Lunar and Planetary Science XXXIX.

Chojnacki M, Burr DM, and Moersch JE (2014a), Valles Marineris dune fields as compared with other Martian populations: Diversity of dune compositions, morphologies, and thermophysical properties, Icarus, 230, 96–142.

Chojnacki M, Burr DM, Moersch JE, and Wray JJ (2014b), Valles Marineris dune sediment provenance and pathways, Icarus, 232,187–219.

Christensen PR, Morris RV, Lane MD, Bandfield JL, and Malin MC (2001a), Global mapping of Martian hematite mineral deposits: Remnants of water-driven processes on early Mars, J. Geophys. Res, 106, 23,873–23,885, doi:10.1029/2000JE001415.

Christensen PR, et al. (2001b), Mars Global Surveyor Thermal Emission Spectrometer experiment: Investigation description and surface science results, J. Geophys. Res, 106, 23,823–23,871, doi: 10.1029/2000JE001370.

Christensen PR, et al. (2003), Morphology and composition of the surface of Mars: Mars Odyssey THEMIS results, Science, 300, 2056–2061, doi:10.1126/science.1080885. [PubMed: 12791998]

Christensen PR, Jakosky BM, Kieffer HH, Malin MC, McSween HY, Nealson K, Mehall GL, Silverman SH, Ferry S, and Caplinger M (2004), The Thermal Emission Imaging System (THEMIS) for the Mars 2001 Odyssey mission, Space Sci. Rev, 110(1), 85–130.

Christensen PR, Engle E, Anwar S, Dickenshied S, Noss D, Gorelick N, and Weiss-Malik M (2009), JMARS—A planetary GIS, paper presented at 2009 Fall Meeting, AGU, San Francisco, Calif.

Daval D, Sissmann O, Corsvisier J, Garcia B, Martinez I, Guyot F, and Hellman R (2010), The effect of silica coatings on the weathering rates of wollastonite (CaSiO3) and forsterite (Mg2SiO4): An apparent paradox? in Water-Rock Interaction, edited by Birkle P and Torres- Alavrado IS, pp. 713–716, Taylor and Francis, London.

Daval D, et al. (2011), Influence of amorphous silica layer formation on the dissolution rate of olivine at90°C and elevated pCO2, Chem. Geol, 284(1), 193–209.

Edwards CS, and Ehlmann BL (2015), Carbon sequestration on Mars, Geology, 43(10), 863–866.

Edwards CS, Nowicki KJ, Christensen PR, Hill J, Gorelick N, and Murray K (2011), Mosaicking of global planetary image datasets: 1. Techniques and data processing for Thermal Emission Imaging System (THEMIS) multi-spectral data, J. Geophys. Res, 116, E10008, doi: 10.1029/2010JE003755.

Ehlmann BL, and Edwards CS (2014), Mineralogy of the Martian surface, Annu. Rev. Earth Planet. Sci, 42(1), 291–315.

Ehlmann BL, et al. (2008), Orbital identification of carbonate-bearing rocks on Mars, Science, 322,1828–1832, doi:10.1126/science.1164759. [PubMed: 19095939]

Ehlmann BL, et al. (2009), Identification of hydrated silicate minerals on Mars using MRO-CRISM: Geologic context near Nili Fossae and implications for aqueous alteration, J. Geophys. Res, 114, E00D08, doi:10.1029/2009JE003339.

Feely KC, and Christensen PR (1999), Quantitative compositional analysis using thermal emission spectroscopy: Application to igneous and metamorphic rocks, J. Geophys. Res, 104, 24,195–24,210, doi:10.1029/1999JE001034.

Fenton LK, Bandfield JL, and Ward AW (2003), Aeolian processes in Proctor Crater on Mars: Sedimentary history as analyzed from multiple data sets, J. Geophys. Res, 108(E12), 5129, doi: 10.1029/2002JE002015.

Fergason RL, Christensen PR, and Kieffer HH (2006), High-resolution thermal inertia derived from the Thermal Emission Imaging System (THEMIS): Thermal model and applications, J. Geophys. Res, 111, E12004, doi:10.1029/2006JE002735.

Gillespie AR, Kahle AB, and Walker RE (1986), Color enhancement of highly correlated images: I. Decorrelation and HSI contrast stretches, Remote Sens. Environ, 20, 209–235.

Goudge TA, Mustard JF, Head JW, Fassett CI, and Wiseman SM (2015), Assessing the mineralogy of the watershed and fan deposits of the Jezero crater paleolake system, Mars, J. Geophys. Res. Planets, 120, 775–808, doi:10.1002/2014JE004782.

Hamilton VE, and Christensen PR (2000), Determining the modal mineralogy of mafic and ultramafic igneous rocks using thermal emission spectroscopy, J. Geophys. Res, 105, 9717–9733, doi: 10.1029/1999JE001113.

Hamilton VE, and Christensen PR (2005), Evidence for extensive, olivine-rich bedrock on Mars, Geology, 33(6), 433–436, doi:10.1130/G21258.1.

Hamilton VE, Christensen PR, McSween HY Jr., and Bandfield JL (2003), Searching for the source regions of Martian meteorites using MGS TES: Integrating Martian meteorites into the global distribution of volcanic materials on Mars, Meteorit. Planet. Sci, 38(6), 871–885.

Hamilton VE, et al. (2014), Observations and preliminary science results from the first 100 sols of MSL REMS ground temperature sensor measurements at Gale Crater, J. Geophys. Res. Planets, 119, 745–770, doi:10.1002/2013JE004520.

Hoefen TM, Clark RN, Bandfield JL, Smith MD, Pearl JC, and Christensen PR (2003), Discovery ofolivine in the Nili Fossae region of Mars, Science, 302, 627–630. [PubMed: 14576430]

Hurowitz JA, McLennan SM, Tosca NJ, Arvidson RE, Michalski JR, Ming DW, Schröder C, and Squyres SW (2006), In situ and experimental evidence for acidic weathering of rocks and soils on Mars, J. Geophys. Res, 111, E02S19, doi:10.1029/2005JE002515.

Jakosky BM (1979), The effects of non-ideal surfaces on the derived thermal properties of Mars, J. Geophys. Res, 84, 8252–8262, doi:10.1029/JB084iB14p08252.

Kieffer HH (2013), Thermal model for analysis of Mars infrared mapping, J. Geophys. Res. Planets, 118,451–470, doi:10.1029/2012JE004164.

Koeppen WC, and Hamilton VE (2008), Global distribution, composition, and abundance of olivine on the surface of Mars from thermal infrared data, J. Geophys. Res, 113, E05001, doi: 10.1029/2007JE002984.

Kraft MD, Michalski JR, and Sharp TG (2003), Effects of pure silica coatings on thermal emission spectra of basaltic rocks: Considerations for Martian surface mineralogy, Geophys. Res. Lett, 30(24), 2288, doi:10.1029/2003GL018848.

Lasaga AC (1984), Chemical kinetics of water-rock interactions, J. Geophys. Res, 89,4009–4025, doi: 10.1029/JB089iB06p04009.

Lyon RJP (1964), Evaluation of infrared spectrophotometry for compositional analysis of lunar and planetary soils: II. Rough and powdered surfaces, NASA Contract. Rep. CR-100, 175 pp., Stanford Res. Inst., Palo Alto, Calif.

Malin MC, et al. (2007), Context camera investigation on board the Mars Reconnaissance Orbiter, J. Geophys. Res, 112, E05S04, doi:10.1029/2006JE002808.

Mangold N, Baratoux D, Arnalds O, Bardintzeff JM, Platevoet B, Grégoire M, and Pinet P (2011), Segregation of olivine grains in volcanic sands in Iceland and implications for Mars, Earth Planet. Sci. Lett, 310(3–4), 233–243.

Martin TZ (1986), Thermal infrared opacity of the Mars atmosphere, Icarus, 66, 2–21.

McDowell ML, and Hamilton VE (2007), Geologic characteristics of relatively high thermal inertia intracrater deposits in southwestern Margaritifer Terra, Mars, J. Geophys. Res, 112, E12001, doi: 10.1029/2007JE002925.

McEwen AS, et al. (2007), Mars Reconnaissance Orbiter's High Resolution Imaging Science Experiment (HiRISE), J. Geophys. Res, 112, E05S02, doi:10.1029/2005JE002605.

McLennan SM, et al. (2014), Elemental geochemistry of sedimentary rocks at Yellowknife Bay, Gale Crater, Mars, Science, 343(6169), 1244734. [PubMed: 24324274]

McSween HY Jr., Taylor GJ, and Wyatt MB (2009), Elemental composition of the Martian crust, Science, 324, 736–739. [PubMed: 19423810]

Mellon MT, Jakosky BM, Kieffer HH, and Christensen PR (2000), High-resolution thermal inertia mapping from the Mars Global Surveyor Thermal Emission Spectrometer, Icarus, 148(2), 437–455.

Michalski JR, Kraft MD, Sharp TG, and Christensen PR (2006), Effects of chemical weathering on infrared spectra of Columbia River Basalt and spectral interpretations of Martian alteration, Earth Planet. Sci. Lett, 248, 822–829, doi:10.1016/j.epsl.2006.06.034.

Ming D, et al. (2006), Geochemical and mineralogical indicators for aqueous processes in the Columbia Hills of Gusev crater, Mars, J. Geophys. Res, 111, E02S12, doi:10.1029/2005JE002560.

Mustard JF, et al. (2008), Hydrated silicate minerals on Mars observed by the Mars Reconnaissance Orbiter CRISM instrument, Nature, 454(7202), 305–309, doi:10.1038/nature07097. [PubMed: 18633411]

Mustard JF, Ehlmann B, Murchie S, Poulet F, Mangold N, Head J, Bibring JÄ, and Roach L (2009), Composition, morphology, and stratigraphy of Noachian crust around the Isidis basin, J. Geophys. Res, 114, E00D12, doi:10.1029/2009JE003349.

Nowicki SA, and Christensen PR (2007), Rock abundance on Mars from the Thermal Emission Spectrometer, J. Geophys. Res, 112, E05007, doi:10.1029/2006JE002798.

Ody A, Poulet F, Langevin Y, Bibring JP, Bellucci G, Altieri F, Gondet B, Vincendon M, Carter J, and Manaud NCEJ (2012), Global maps of anhydrous minerals at the surface of Mars from OMEGA/MEx, J. Geophys. Res, 117, E00J14, doi:10.1029/2012JE004117.

Ody A, Poulet F, Bibring JP, Loizeau D, Carter J, Gondet B, and Langevin Y (2013), Global investigation of olivine on Mars: Insights into crust and mantle compositions, J. Geophys. Res. Planets, 118, 234–262, doi:10.1029/2012JE004149.

Pelkey SM, et al. (2007), CRISM multispectral summary products: Parameterizing mineral diversity on Mars from reflectance, J. Geophys. Res, 112, E08S14, doi:10.1029/2006JE002831.

Piqueux S, and Christensen PR (2009), A model of thermal conductivity for planetary soils: 2. Theory for cemented soils, J. Geophys. Res, 114, E09006, doi:10.1029/2008JE003309.

Presley MA, and Christensen PR (1997), Thermal conductivity measurements of particulate materials. Part I: A review, J. Geophys. Res, 102, 6535–6549, doi:10.1029/96JE03302.

Putzig NE, and Mellon MT (2007a), Thermal behavior of horizontally mixed surfaces on Mars, Icarus, 191, 52–67.

Putzig NE, and Mellon MT (2007b), Apparent thermal inertia and the surface heterogeneity of Mars, Icarus, 191, 68–94.

Putzig NE, Barratt EM, Mellon MT, and Michaels TI (2013), MARSTHERM: A web-based system providing thermophysical analysis tools for Mars research, Abstract #P43C-2023 presented at 2013 Fall Meeting, AGU.

Rampe EB, Kraft MD, and Sharp TG (2013), Deriving chemical trends from thermal infrared spectra of weathered basalt: Implications for remotely determining chemical trends on Mars, Icarus, 225(1), 749–762.

Ramsey MS, and Christensen PR (1998), Mineral abundance determination: Quantitative deconvolution of thermal emission spectra, J. Geophys. Res, 103, 577–596, doi:10.1029/97JB02784.

Rogers AD, and Aharonson O (2008), Mineralogical composition of sands in Meridiani Planum determined from Mars Exploration Rover data and comparison to orbital measurements, J. Geophys. Res, 113, E06S14, doi:10.1029/2007JE002995.

Rogers AD, and Bandfield JL (2009), Mineralogical characterization of Mars Science Laboratory candidate landing sites from THEMIS and TES data, Icarus, 203(2), 437–453.

Rogers AD, and Christensen PR (2007), Surface mineralogy of Martian low-albedo regions from MGS-TES data: Implications for upper crustal evolution and surface alteration, J. Geophys. Res, 112, E01003, doi:10.1029/2006JE002727.

Rogers AD, and Hamilton VE (2015), Compositional provinces of Mars from statistical analyses of TES, GRS, OMEGA, and CRISM data, J. Geophys. Res. Planets, 120, 62–91, doi:10.1002/2014JE004690.

Ruff SW, and Christensen PR (2002), Bright and dark regions on Mars: Particle size and mineralogical characteristics based on Thermal Emission Spectrometer data, J. Geophys. Res, 107(E12), 5127, doi:10.1029/2001JE001580.

Salvatore MR, Mustard J, Wyatt M, and Murchie SL (2010), Definitive evidence of Hesperian basalt in Acidalia and Chryse planitiae, J. Geophys. Res, 115, E07005, doi:10.1029/2009JE003519.

Schneider RD, and Hamilton VE (2006), Evidence for locally derived, ultramafic intracrater materials in Amazonis Planitia, Mars, J. Geophys. Res, 111, E09007, doi:10.1029/2005JE002611.

Squyres SW, and Knoll AH (2005), Sedimentary rocks at Meridiani Planum: Origin, diagenesis, and implications for life on Mars, Earth Planet. Sci. Lett, 240(1), 1–10.

Squyres SW, et al. (2004), In situ evidence for an ancient aqueous environment at Meridiani Planum, Mars, Science, 306, 1709–1714. [PubMed: 15576604]

Stockstill-Cahill KR, Anderson FS, and Hamilton VE (2008), A study of low albedo deposits within Amazonis Planitia craters: Evidence for locally-derived ultramafic to mafic materials, J. Geophys. Res, 113, E07008, doi:10.1029/2007JE003036.

Stopar JD,Taylor GJ, Hamilton VE, and Browning L (2006), Kinetic model of olivine dissolution and extent of aqueous alteration on Mars, Geochim. Cosmochim. Acta, 70, 6136–6152.

Thomson JL, and Salisbury JW (1993), The mid-infrared reflectance of mineral mixtures (7–14 μm), Remote Sens. Environ, 45, 1–13.

Tirsch D, Jaumann R, Pacifici A, and Poulet F (2011), Dark aeolian sediments in Martian craters: Composition and sources, J. Geophys. Res, 116, E03002, doi:10.1029/2009JE003562.

Tornabene LL, Moersch JE, McSween HY, Hamilton VE, Piatek JL, and Christensen PR (2008), Surface and crater-exposed lithologic units of the Isidis Basin as mapped by coanalysis of THEMIS and TES derived data products, J. Geophys. Res, 113, E10001, doi: 10.1029/2007JE002988.

Viviano-Beck CE, et al. (2014), Revised CRISM spectral parameters and summary products, paper presented at Lunar and Planetary Science Conference XLV, The Woodlands, Tex.

Key Points:

- Olivine-bearing materials on Mars display a wide range of thermal inertias
- TES data indicate that olivine-rich (>25%) materials commonly have apparent thermal inertias <400 J m^{-2} K^{-1} $s^{-1/2}$
- Correlation between olivine abundance and thermal inertia alone cannot be used to infer olivine chemical weathering in the examined areas

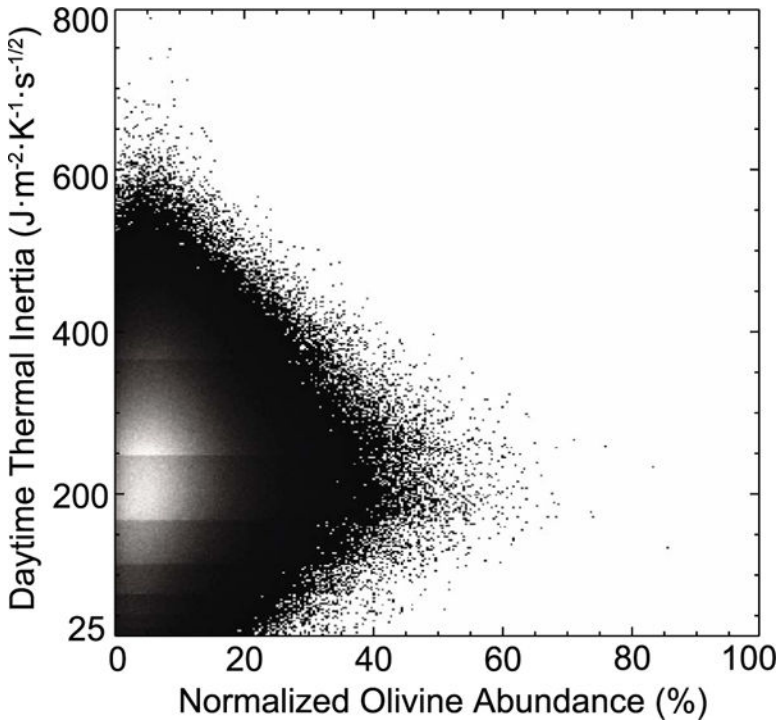

Figure 1.

TES-derived daytime thermal inertia and total normalized olivine abundance plotted for each data point. Lighter colors represent greater data density. There is a wide range of olivine abundances for all thermal inertia surfaces.

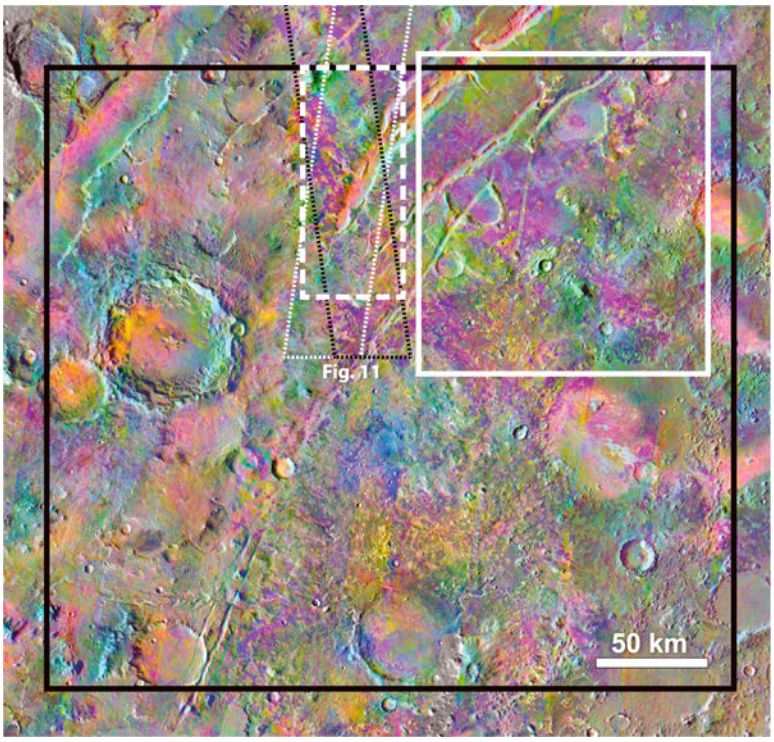

Figure 2.

The 8–7–5 DCS mosaic daytime THEMIS images of Nili Fossae region. Center of image is 20.6°N, 77.6°E. Solid and dashed boxes define three ROIs: large (black), medium (white solid), and small (white dash). Locations of THEMIS images in Figure 11a are shown as white (daytime) and black (nighttime) dotted outlines.

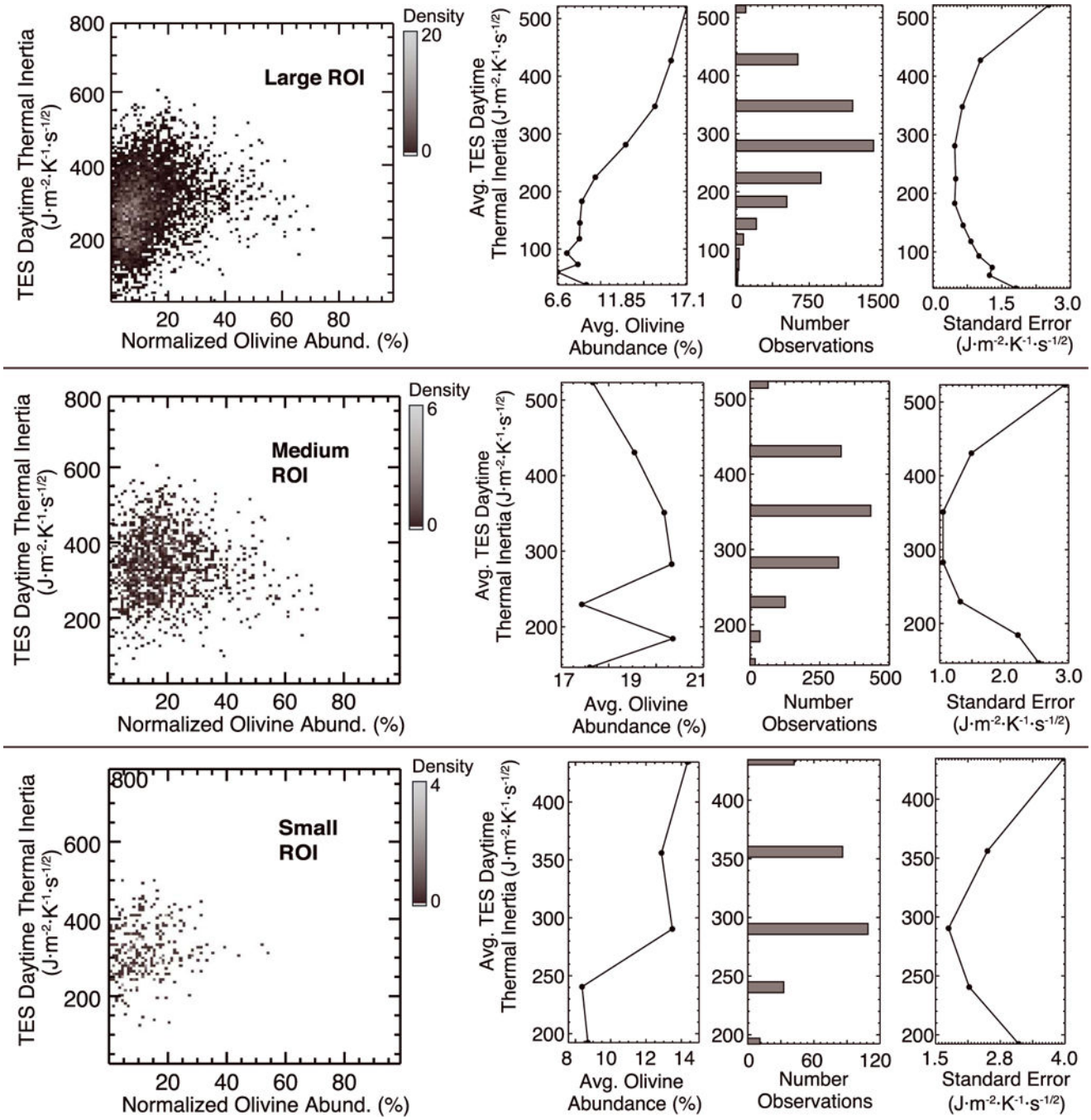

Figure 3.

Nili Fossae TES-derived daytime thermal inertia versus normalized olivine abundance. (left column) Density plots and (second to fourth columns) binned thermal inertia data with average olivine abundance, for the three ROIs in Figure 2. The density plots for the all three ROIs indicate that for all olivine abundances (0–70%) there exist a wide range of thermal inertias (0–600 J m^{-2} K^{-1} $s^{-1/2}$) and a particular relationship between thermal inertia and olivine abundance is not apparent. When the data are binned (Figure 3, second to fourth

columns), the large and small ROIs show a generally positive correlation between thermal inertia and olivine abundance, while the medium ROI does not.

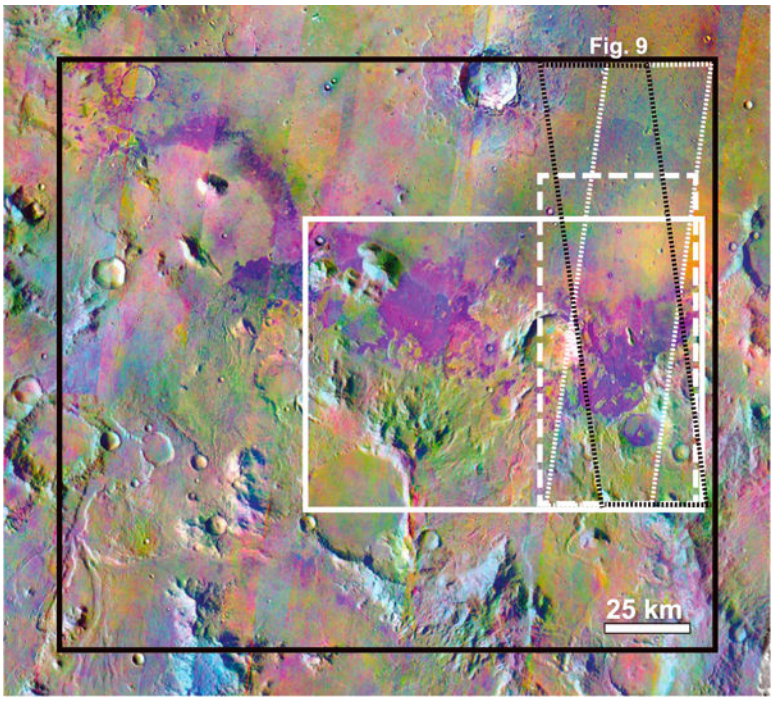

Figure 4.

The 8–7–5 DCS mosaic of daytime THEMIS images of southern Isidis region. Center of image is 3.7°N, 83.8°E. Solid and dashed boxes define three ROIs: large (black), medium (white solid), and small (white dash). Locations of THEMIS images in Figure 9 are shown as white (daytime) and black (nighttime) dotted outlines.

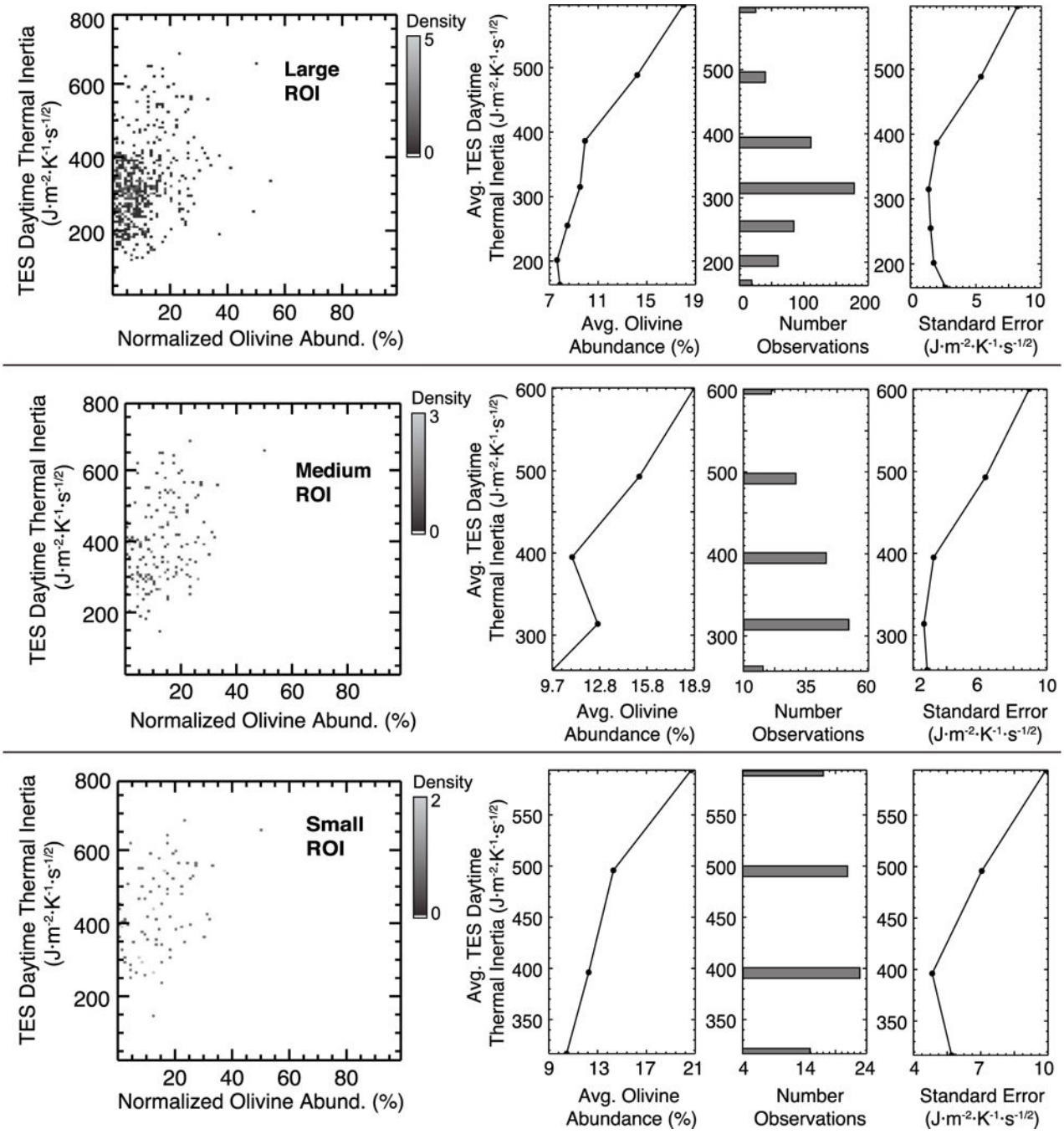

Figure 5.

Southern Isidis TES-derived daytime thermal inertia versus normalized olivine abundance. (left column) Density plots and (second to fourth columns) binned thermal inertia data with average olivine abundance, for the three ROIs in Figure 4. The density plots for all ROIs indicate that there is a large range of thermal inertias (~100–700J m^{-2} K^{-1} $s^{-½}$) for nearly all olivine abundances (0–60%). The binned data indicate a generally positive correlation between thermal inertia and olivine abundance for all three ROIs.

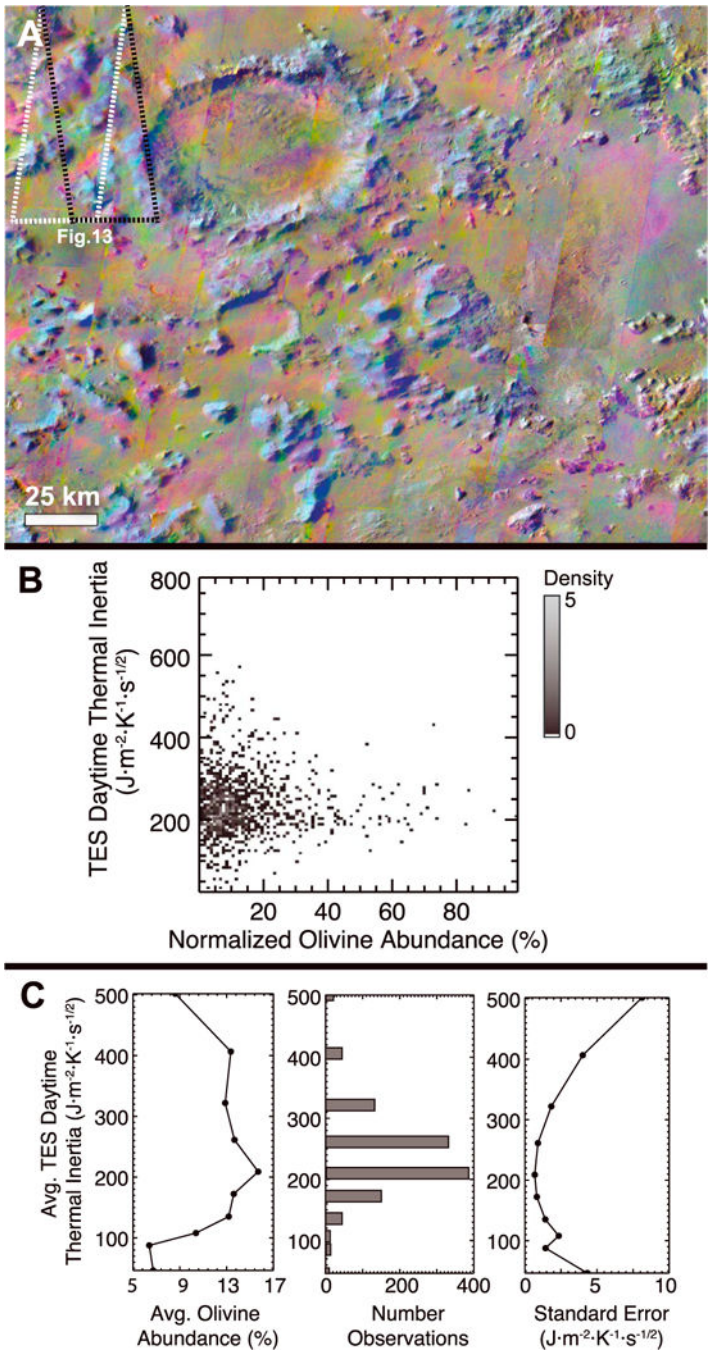

Figure 6.

(a) The 8–7–5 DCS mosaic of daytime THEMIS images for Argyre Planitia. The entire image represents ROI, and the center of the image is −45.2°N, 328.6°E. Locations of THEMIS images in Figure 13 are shown as white (daytime) and black (nighttime) dotted outlines. (b) Density plot of TES-derived daytime thermal inertia and normalized olivine abundance. The normalized olivine abundances (0–90%) show a large spread in thermal inertia (0–580 J m^{-2} K^{-1} $s^{-1/2}$), but the highest olivineabundances(>40%) generally have more limited thermal inertias (100–430 J m^{-2} K^{-1} $s^{-1/2}$). (c) Binned thermal inertia with

average olivine abundance for Argyre Planitia. Argyre Planitia shows a complex relationship between thermal inertia and olivine abundance with a peak in average olivine abundance at ~188–235 J m^{-2} K^{-1} $s^{-1/2}$.

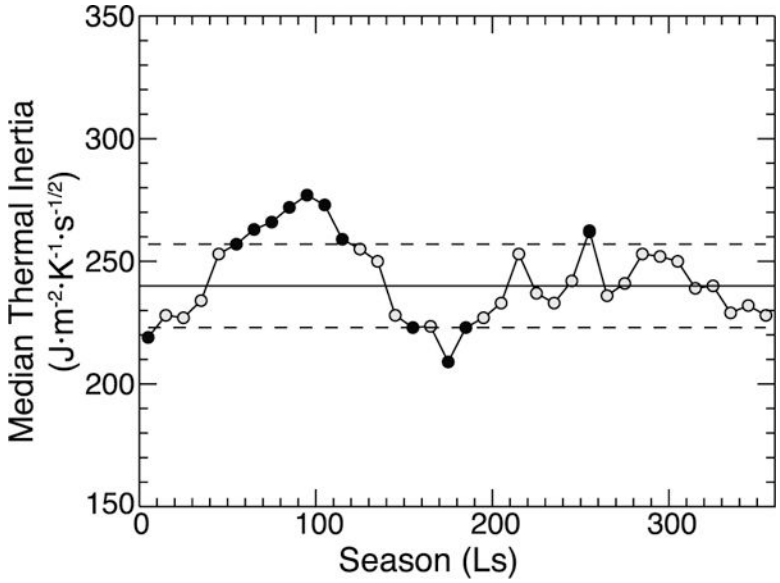

Figure 7.

Median TES daytime thermal inertia of Nili Fossae region per 10° L_S. The solid line is the median thermal inertia of all seasonal medians, and the dashed lines mark one standard deviation above and below the median. Black dots are seasonal median thermal inertias that lie outside this range.

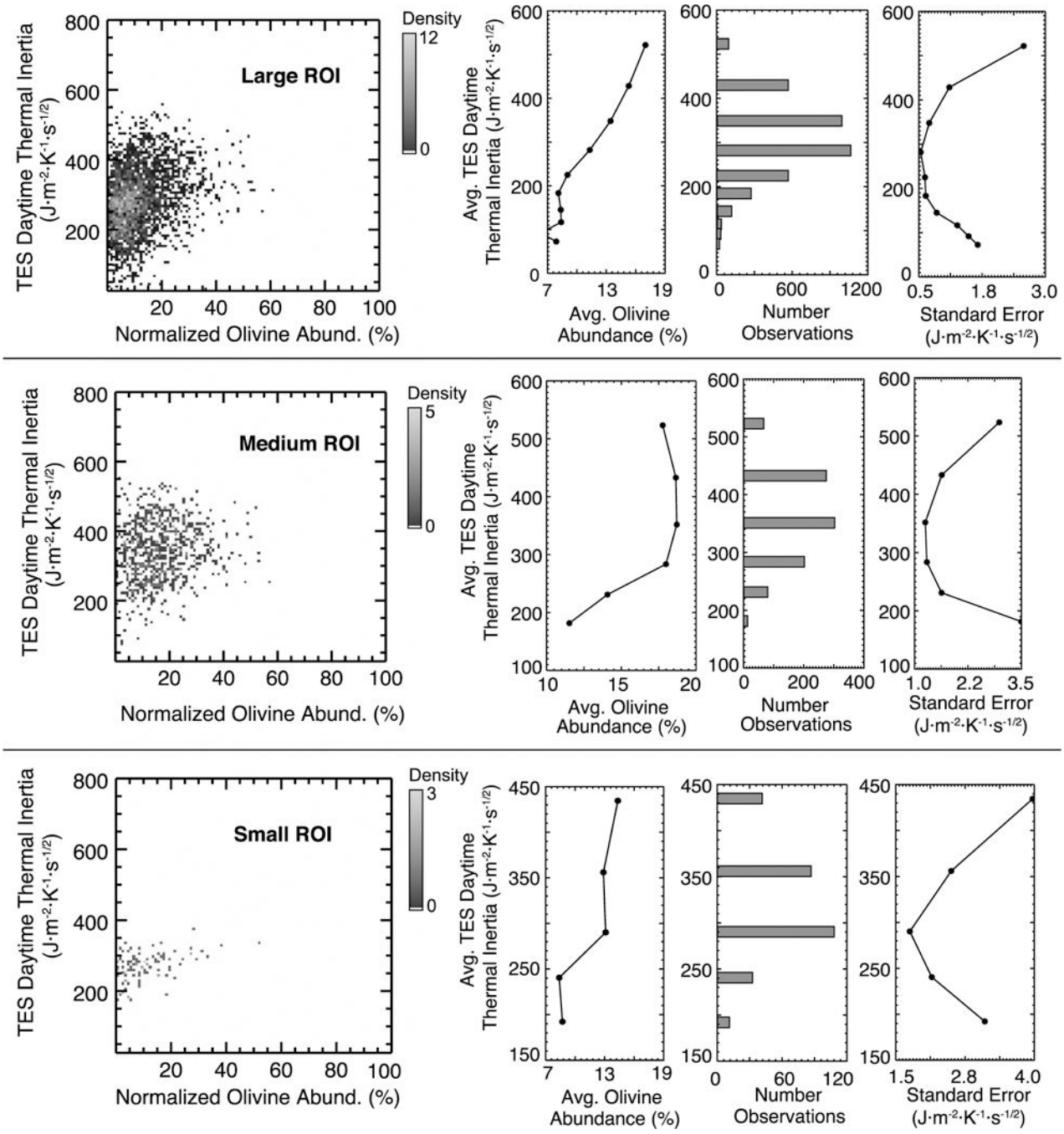

Figure 8.

Nili Fossae TES-derived daytime thermal inertia versus normalized olivine abundance. (left column) Density plots and (second to fourth columns) binned thermal inertia data with average olivine abundance, for the three ROIs in Figure 2 using only limited seasonal TES data (Figure 7). The density plots are generally unchanged from the all-data case (Figure 3) with all ROIs displaying a wide range of thermal inertias for nearly all olivine abundances, but some small changes are apparent (compare to Figure 3). The binned data (Figure 8, second to fourth columns) indicate however that the general relationship between thermal

inertia and olivine abundance did not change. The large and small ROIs still show a generally positive correlation between thermal inertia and olivine abundance, while the medium ROI does not (compare to Figure 3).

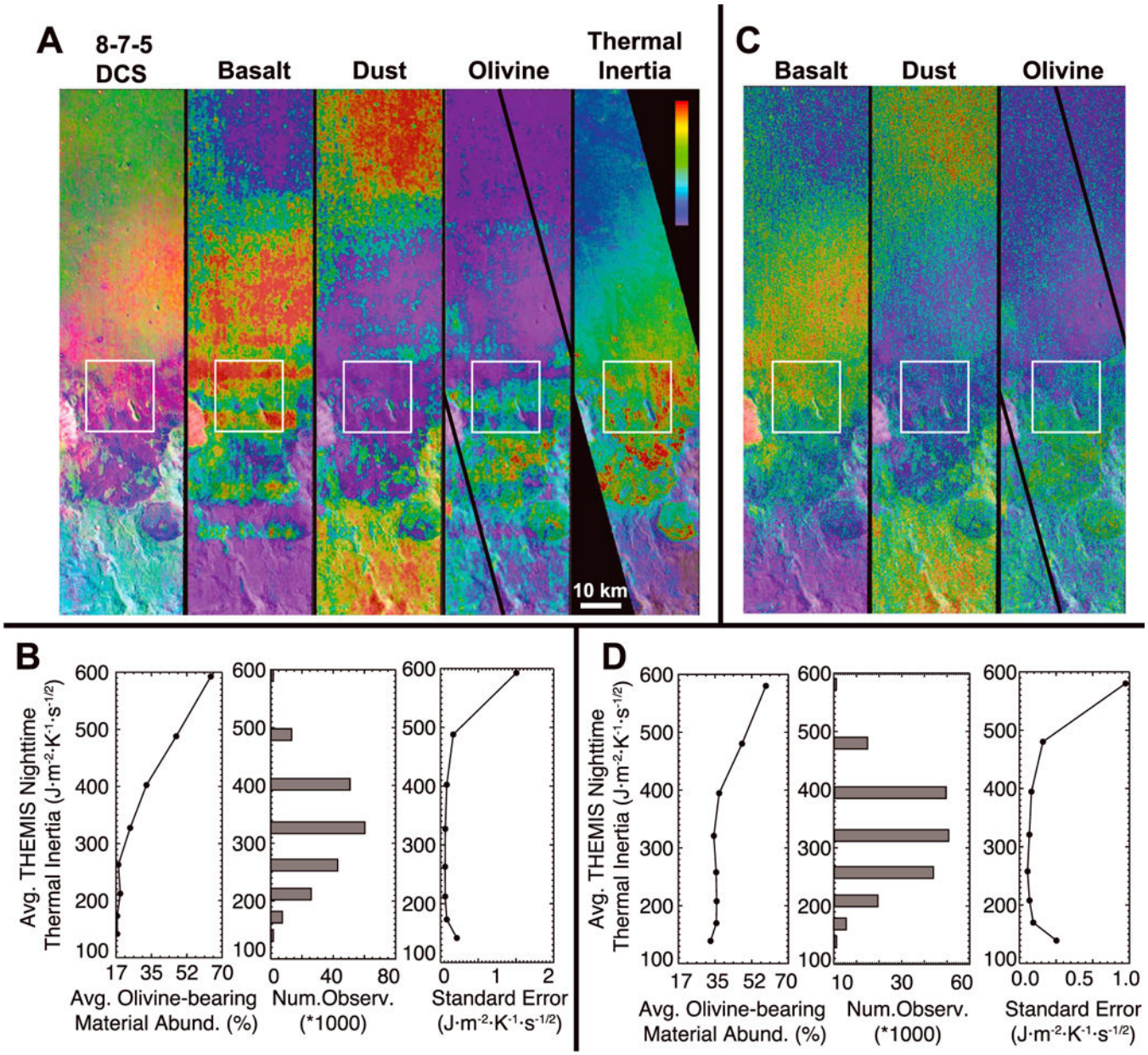

Figure 9.

Southern Isidis. (a) THEMIS daytime image I01395005 8–7–5 DCS, modeled end-members ("olivine" = olivine-bearing material), and overlapping thermal inertia from THEMIS nighttime image I19050003. A noise removal filter has been applied to the daytime THEMIS image prior to atmospheric correction. Color bar for end-member concentrations 0–100% and thermal inertia 150 to 500 J m^{-2} K^{-1} $s^{-1/2}$. Black lines on modeled olivine image outline area of overlap with thermal inertia image. Note the colocation of high olivine-bearing material abundance and high thermal inertia. White boxes show location of CTX image in Figures 10a and 10b. (b) Density-sliced THEMIS-derived thermal inertia bins with average olivine- bearing material abundance confirm a generally positive correlation within the area of overlap. (c) Modeled end-member concentrations for THEMIS image

I01395005 without noise removal filter. Same color bar scale as Figure 9a. General spatial distribution of end-members is unchanged, but modeled amounts have been adjusted with more pixels being modeled as a combination of end-members rather than a pure end-member. Black lines on modeled olivine image outline area of overlap with thermal inertia image in Figure 9a. White boxes show location of CTX image in Figures 10a and 10b. (d) Thermal inertia retains a positive correlation with olivine-bearing material abundance, although the average olivine-bearing material abundance of the lowest thermal inertia bins has increased.

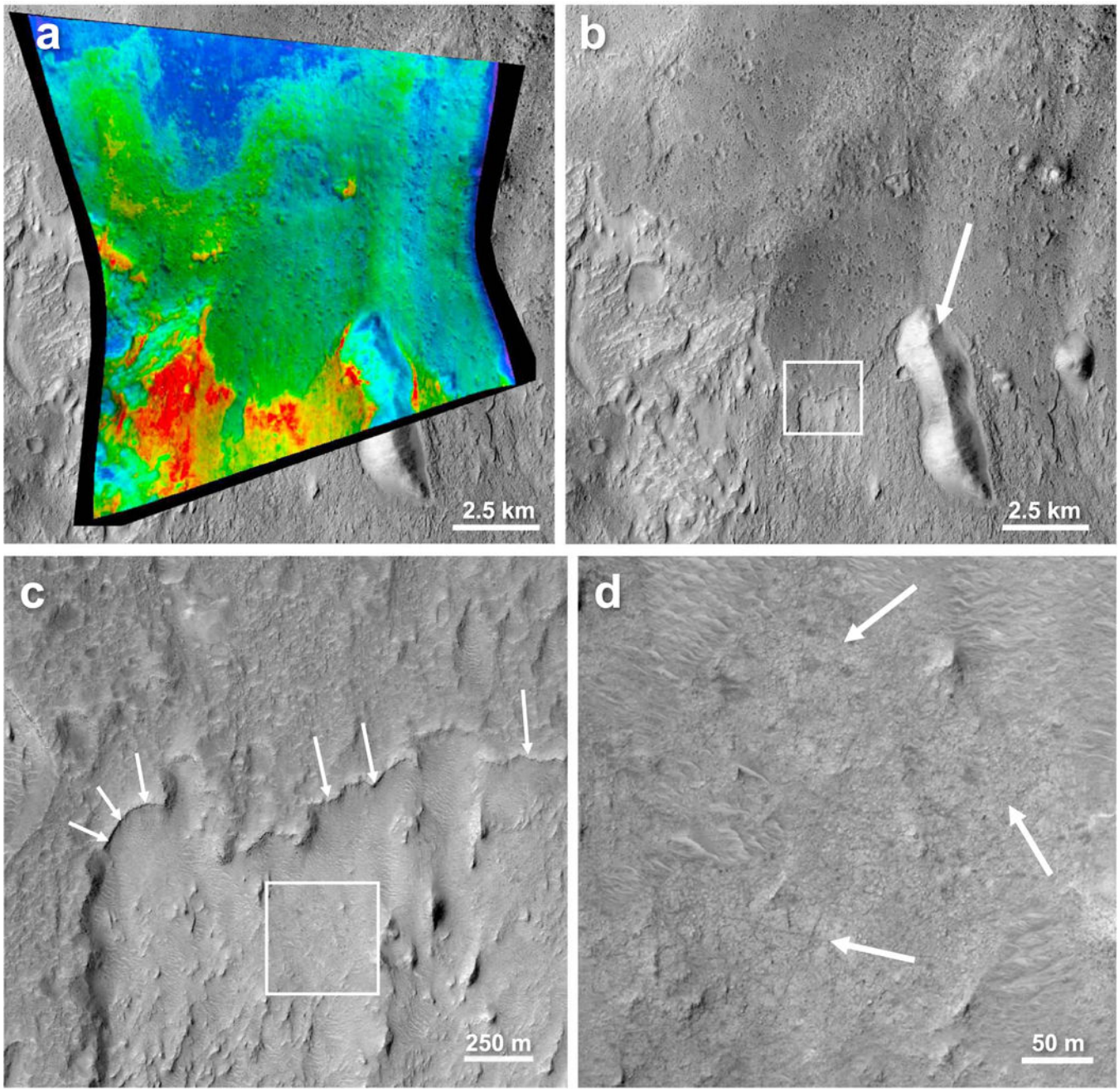

Figure 10.

Southern Isidis. See Figure 9 for image location. (a) CRISM olivine index (OLINDEX2) from image FRT0007F47_07 rendered as a color overlay on gray scale image (average of CRISM bands 350–420) on top of CTX image G22_026649_1835_XN_03N275W. Warmer colors are stronger olivine signatures. Strongest olivine CRISM detections (red) match areas of high abundances of olivine-bearing material modeled by THEMIS (Figure 9). Weakest olivine signatures (green-blue) are modeled as basalt by THEMIS. (b) Portion of CTX image G22_026649_1835_XN_03N275 (same area as in Figure 10a) showing relatively darker-toned and smoother plain unit (basalt) which has a sharp contact with the olivine unit. Note

also the large mound (white arrow) that crops out of the olivine unit and has a much weaker olivine signature (Figure 10a). White box shows location of Figure 10c. (c) Portion of HiRISE image ESP_027005_1835 showing the sharp relief of the upper basalt flow (white arrows) and olivine unit which stratigraphically underlies it. Box shows location of Figure 10 d. (d) Portion of HiRISE image ESP_027005_1835 showing bright-toned coherent, fractured unit (white arrows) that has the strongest olivine signature and is most likely the source of the olivine. Overriding dunes are also present.

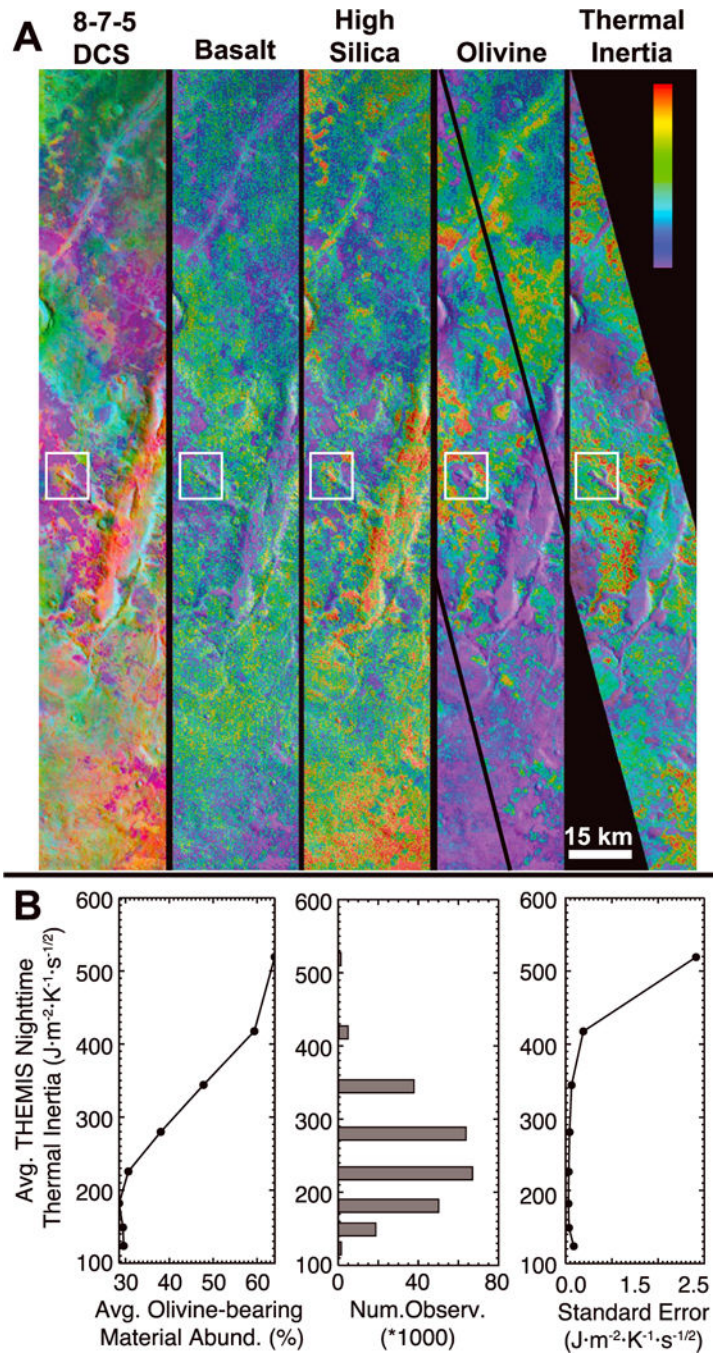

Figure 11.

Nili Fossae. (a) THEMIS daytime image I02007009 8–7-5 DCS, modeled end-members (olivine = olivine-bearing material), and overlapping thermal inertia from THEMIS nighttime image I01327002. Color bar for end-member concentrations 0–100% and thermal inertia 120 to 380 J m^{-2} K^{-1} $s^{-1/2}$. Black lines on modeled olivine image outline area of overlap with thermal inertia image. White boxes show location of CRISM image in Figure 12a. (b) THEMIS-derived thermal inertia bins with average olivine abundance indicate a

generally positive correlation between thermal inertia and olivine abundance within the area of overlap.

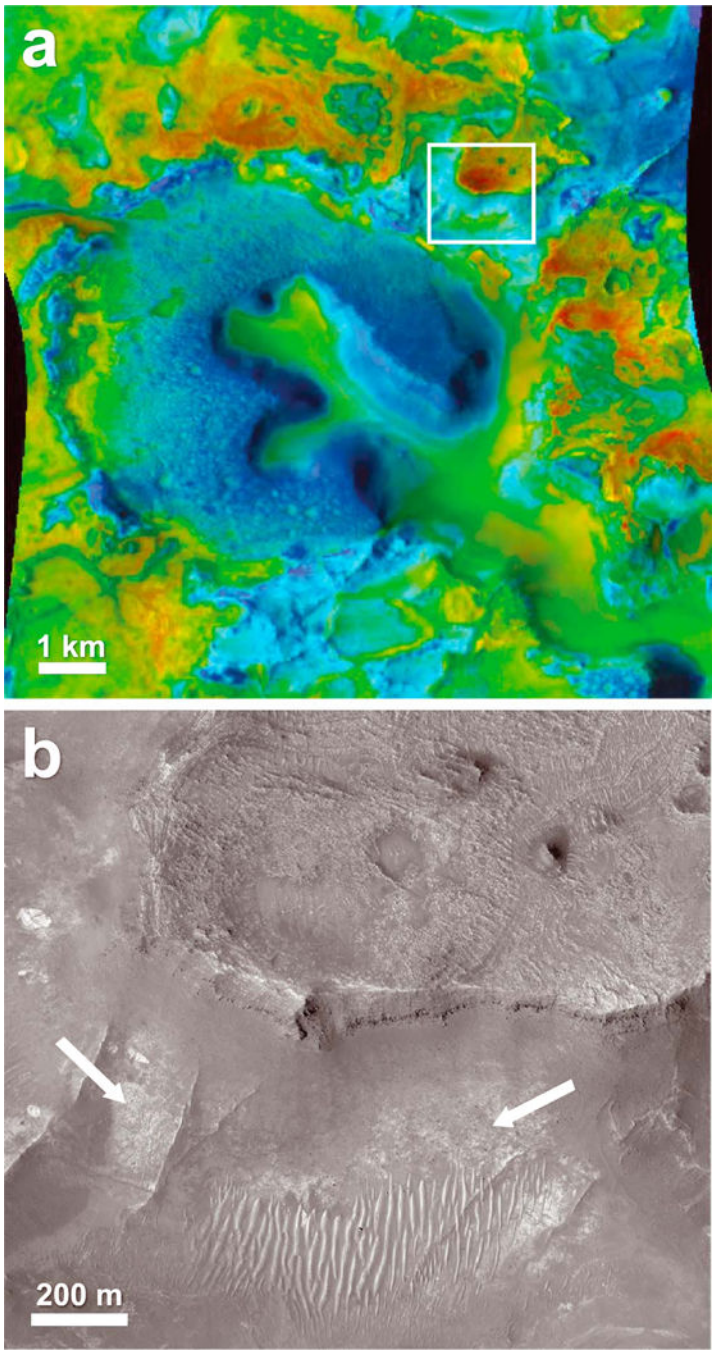

Figure 12.

Nili Fossae. (a) CRISM olivine index (OLINDEX2) from image FRT00003E12_07 rendered as a color overlay on gray scale image (average of CRISM bands 350–420) in location indicated by white boxes in Figure 11a. Warmer colors are stronger olivine signatures. Strongest olivine CRISM detections (red) match areas of high abundances of olivine-bearing material modeled by THEMIS (Figure 12a). Weakest olivine signatures (blue) are modeled as basalt and high silica by THEMIS. White box shows location of Figure 12b. (b) Portion of HiRISE image PSP_002888_2025_RED. Olivine-rich unit (top of image)

stratigraphically overlies a coherent, bright-toned unit with a massive appearance (white arrows) with a weaker olivine signature. The dunes overlying this massive bright-toned unit (bottom center of image) have a relatively stronger olivine signature (green/yellow) according to CRISM. See text for expanded discussion.

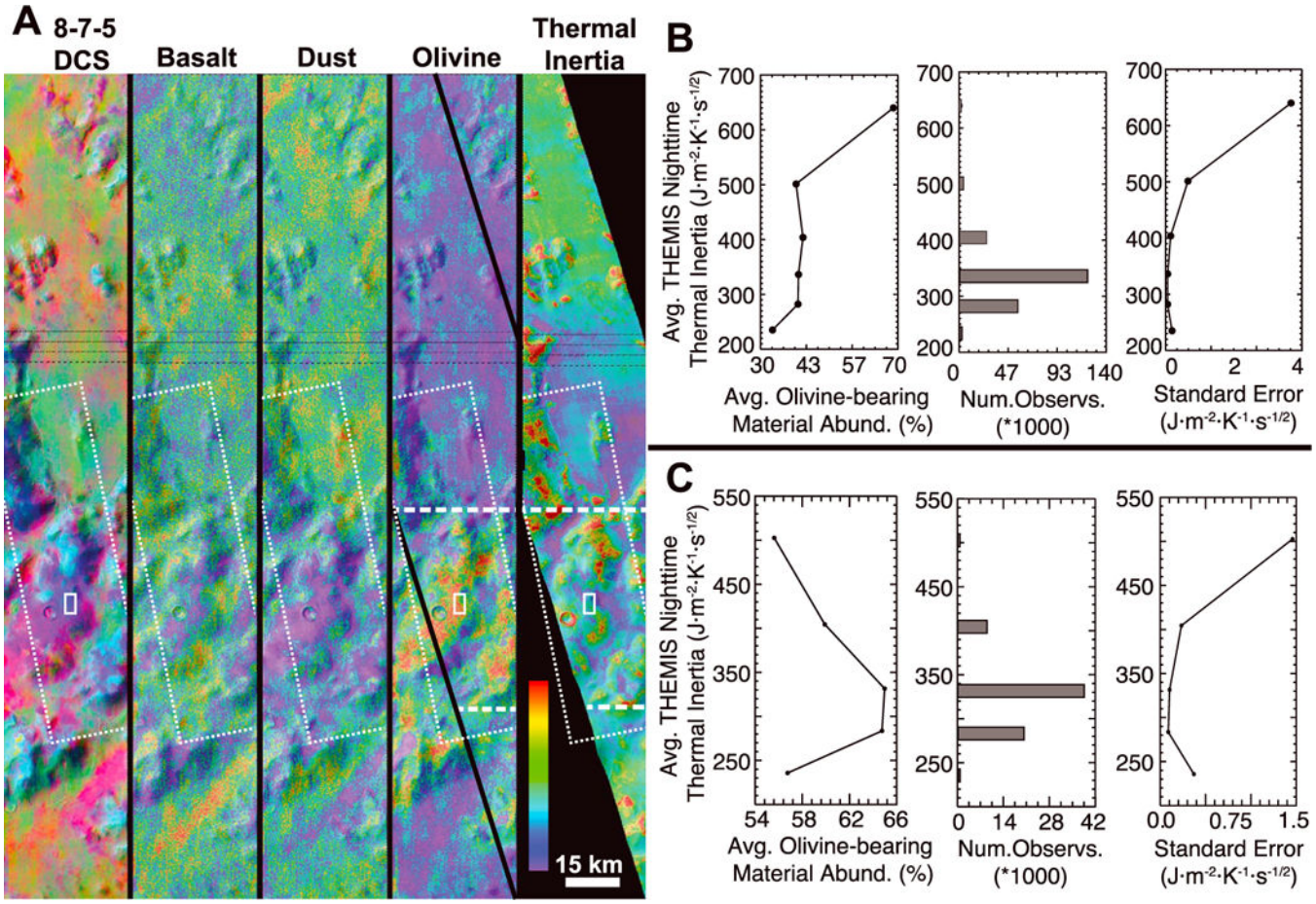

Figure 13.

Argyre Planitia. (a) THEMIS daytime image I41921002 8–7-5 DCS, modeled end-members (olivine = olivine-bearing material), and overlapping thermal inertia from THEMIS nighttime image I34365010. Horizontal black lines on images are dropped (null) lines in THEMIS daytime image (masked in thermal inertia image). Color bar for end-member concentrations 0–100% and thermal inertia 220 to 450J m^{-2} K^{-1} $s^{-1/2}$. Black lines on modeled olivine image outline area of overlap with thermal inertia image. White box shows location of olivine-rich area with average olivine content of 85% and average thermal inertia of 318J m^{-2} K^{-1} $s^{-1/2}$. White dashed lines indicate limited area for plot in Figure 13c. White dotted outlines show location of CTX image in Figure 14a. (b) THEMIS-derived thermal inertia bins with average olivine-bearing material abundance suggest a positive correlation within the entire area of overlap. (c) Analysis limited to area between white dashed lines in Figure 13a. Thermal inertia bin with highest average olivine-bearing material abundance is ~300–376J m^{-2} K^{-1} $s^{-1/2}$, and a simple, positive correlation between thermal inertia and olivine-bearing material abundance is not present.

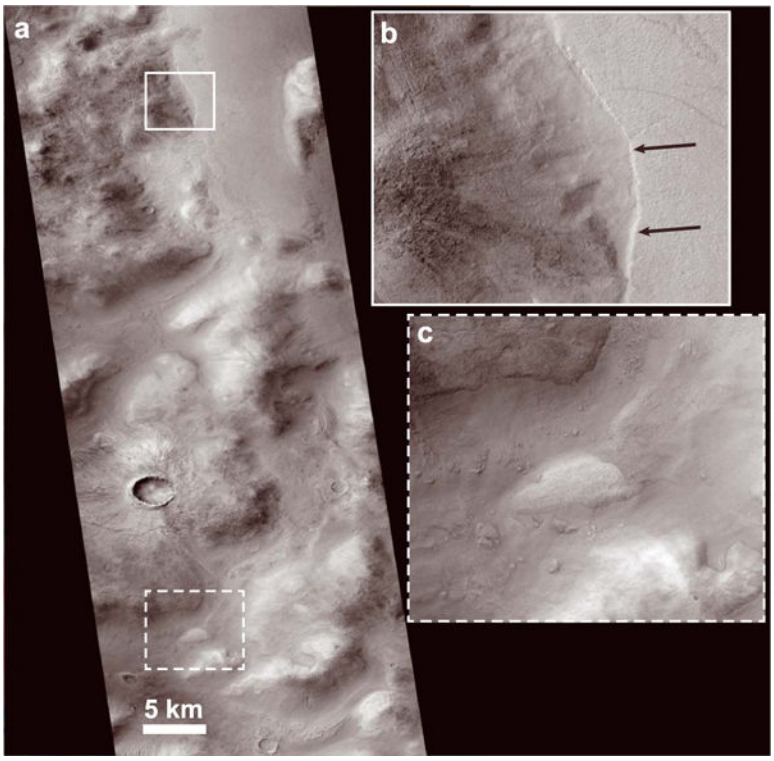

Figure 14.

Argyre. CTX image B12_014298_1373_XI_42S033W. (a) Image over olivine-bearing area (location of image indicated in Figure 13a). Solid white box shows location of Figure 14b, and dashed white box shows location of Figure 14c. North is up in the image, and illumination is from the east. (b) Zoomed area of image showing sharp contact (black arrows) between mound in west and smooth floor to east. Smooth floor unit appears very coherent with a subtle texture at highest resolution. Sharp edge of unit can be traced intermittently around to the west (not shown). Smooth unit is interpreted as a lava flow that has embayed higher topography and is therefore not a weathering product of the surrounding olivine-bearing hills. (c) Zoomed area of image showing outcrop of bright-toned, textured mound in middle of valley between two olivine-rich hills. Mound is not modeled as olivine bearing with THEMIS data (Figure 13) and likely represents separate unit that is not a direct weathering product of olivine-bearing hills.This unit outcrops in several other areas in the valleys between olivine-bearing hills.

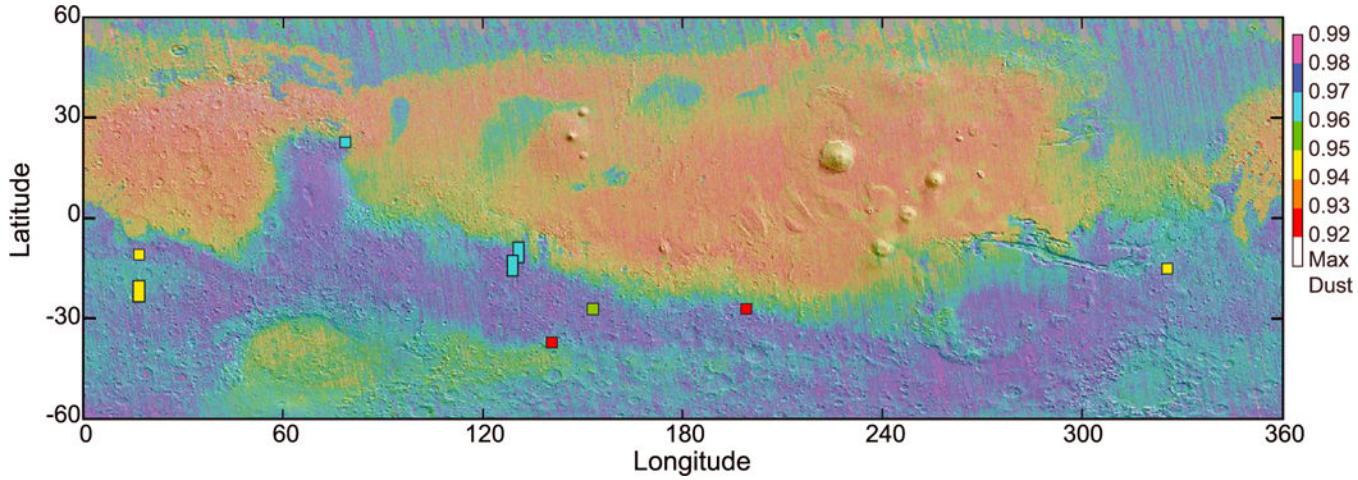

Figure 15.

Mars Orbiter Laser Altimeter topography colored by DCI showing eight locations (colored squares) with highest number of TES detections ≥25% total normalized olivine and daytime thermal inertia ≤350 J m^{-2} K^{-1} $s^{-1/2}$. Red squares are likely anomalous olivine detections, and yellow squares are ambiguous (low thermal inertia/high olivine units could not be clearly mapped at TES or THEMIS scale). The blue squares are interpreted as partially dust-covered, olivine-bearing surfaces, and the green square is the location of olivine-bearing, low thermal inertia unit in Terra Cimmeria (Figures 16 and 17).

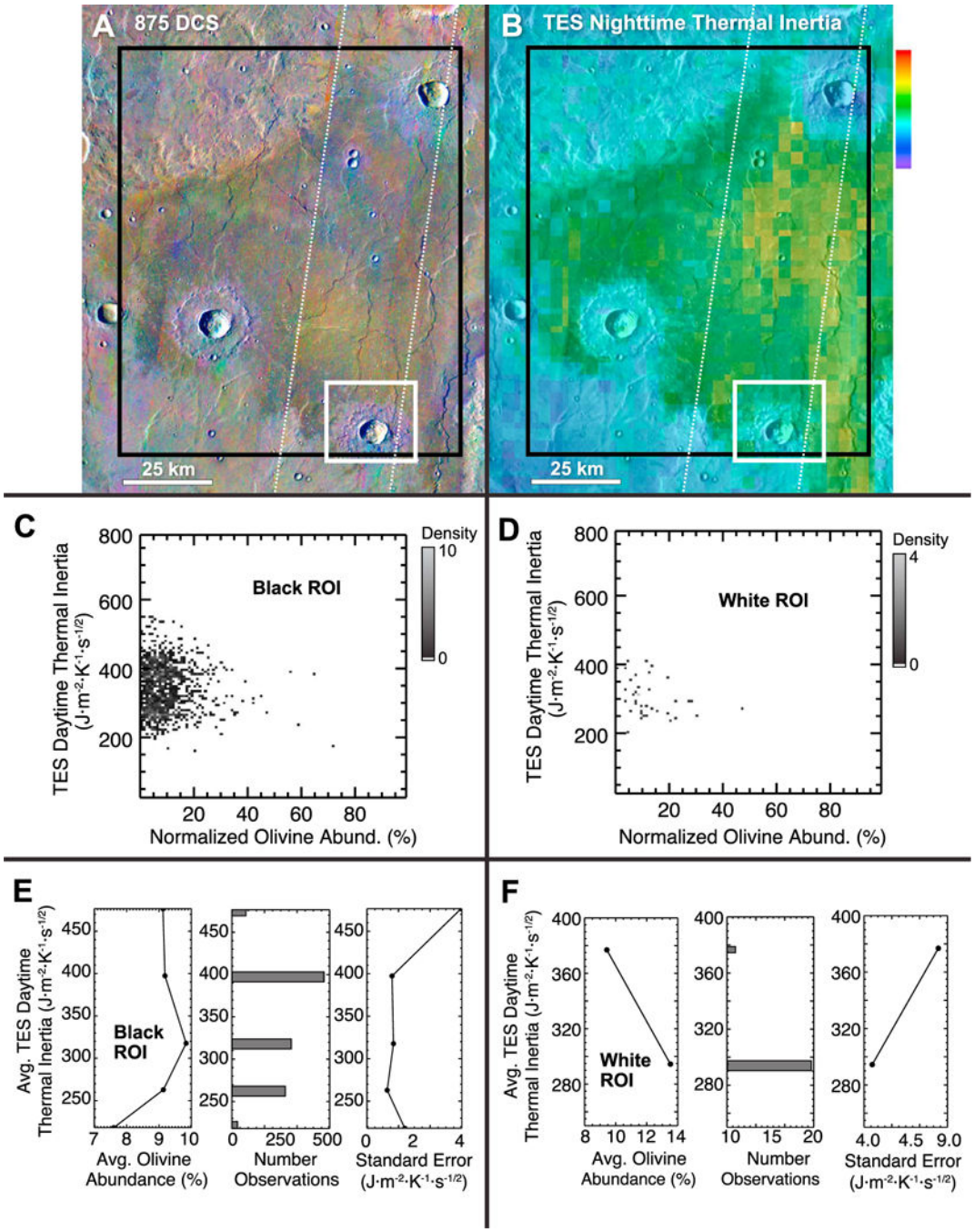

Figure 16.

Terra Cimmeria region showing TES ROIs (solid) and THEMIS image location (dotted) shown in Figure 17. Center of images is 152.9°E, −25.7°N. (a) The 8–7-5 DCS mosaic of THEMIS images. (b) Median TES nighttime thermal inertia from *Putzig and Mellon* [2007a]. Color scalefrom 75 to 600 J m^{-2} K^{-1} $s^{-1/2}$. Crater ejecta have lower thermal inertia and stronger olivine signature (purple in DCS image Figure 16a) than underlying plains. (c) Density plot of TES-derived daytime thermal inertia and normalized olivine abundance for large black ROI (Figures 16a and 16b). (d) Density plot of TES-derived daytime thermal

inertia and normalized olivine abundance for small white ROI (Figures 16a and 16b). (e) Binned thermal inertia with average olivine abundance within black ROI in Figures 16a and 16b. A peak in olivine abundance occurs in the thermal inertia bin 290–310 J m^{-2} K^{-1} $s^{-1/2}$. (f) TES-derived thermal inertia bins with average olivine abundance within small white ROI in Figures 16a and 16b. The lower thermal inertia bin has higher average olivine abundance.

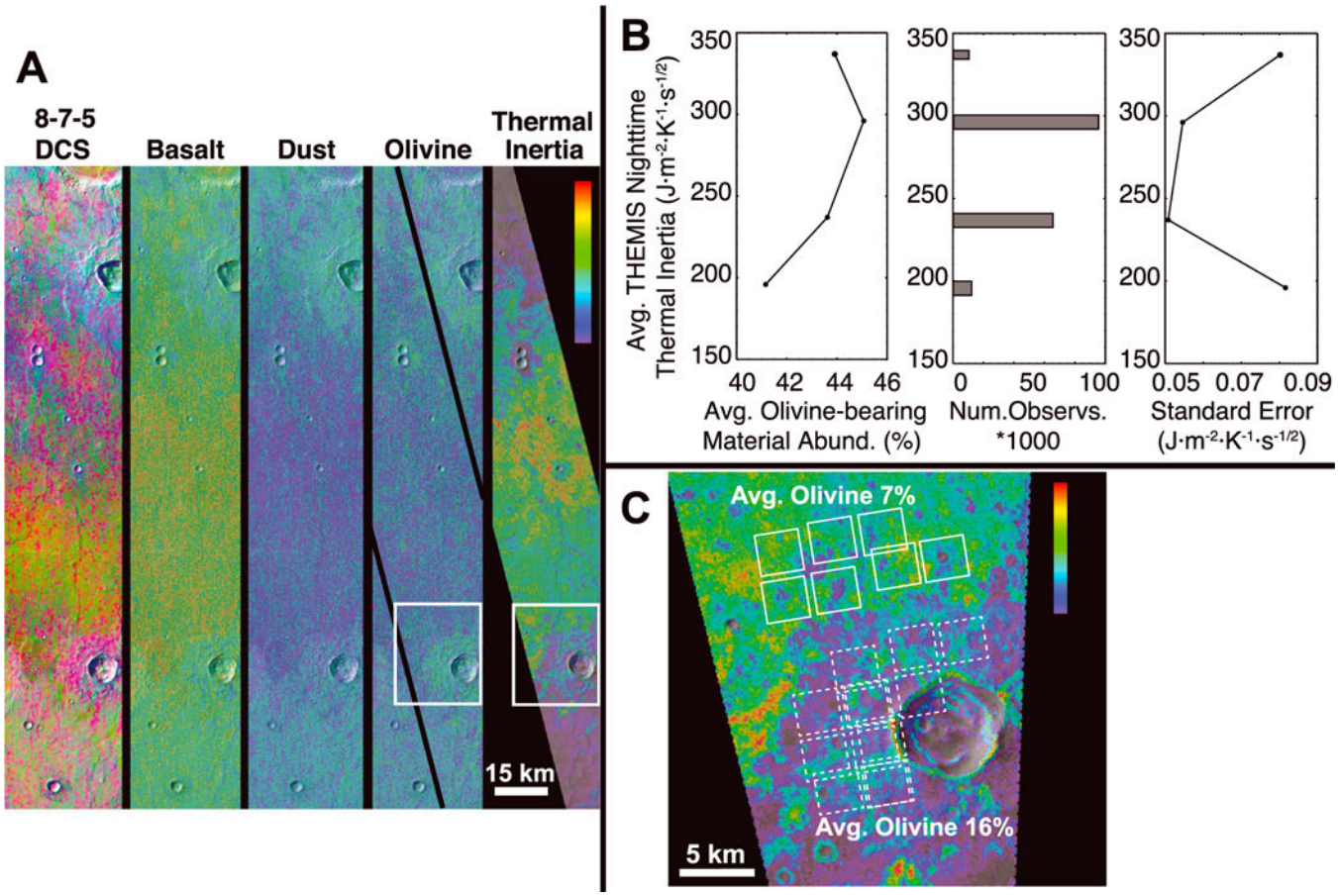

Figure 17.

Terra Cimmeria. (a) THEMIS image I51665002 8–7-5 DCS, modeled end-members (olivine = olivine-bearing material), and overlapping thermal inertia from THEMIS nighttime image I08440010. Color bar applies to end-member concentrations 0–100% and thermal inertia 220 to 360 J m^{-2} K^{-1} $s^{-1/2}$. Majority of the area is modeled as basalt, but crater ejecta show increased modeled olivine compared to plains. White box shows location of Figure 18c. (b) THEMIS-derived density-sliced thermal inertia bins with average olivine-bearing material abundance suggest that thermal inertia bin 262–328 J m^{-2} K^{-1} $s^{-1/2}$ has highest olivine-bearing material abundance. (c) Portion of THEMIS image I08440010 thermal inertia. Color scale from 220 to 360 J m^{-2} K^{-1} $s^{-1/2}$. Boxes show locations of TES pixels used for average thermal inertia and normalized olivine. Crater ejecta (dashed boxes) have lower TES-derived thermal inertia (272 J m^{-2} K^{-1} $s^{-1/2}$) and higher olivine abundance (16%) than underlying plains (solid boxes; 352 J m^{-2} K^{-1} $s^{-1/2}$ and 7%).

Table 1.

Areas Analyazed with TES and THEMIS

Area Label[a]	ROI Extents / Image IDs	Thermal Inertia Range[b]	Avg. Olivine Abundance Range[c]	Figures
		Nili Fossae		
Large ROI[d]	17.97–22.95°N, 279.96–285.47°W	27–611	6.6–17.1%	Figures 2 and 3
Medium ROI[d]	20.49–23.04°N, 280.17–282.49°W	41–611	17.6–20.1%	Figures 2 and 3
Small ROI[d]	21.11 −22.95°N, 282.65–283.42°W	130–505	8.4–14.3%	Figures 2 and 3
Image pair #1	I02007009, I01327002	105–613		Figure 11
		South Isidis		
Large ROI	2.09–5.06°N, 274.88–278.17°W	84–687	7.6–18.0%	Figures 4 and 5
Medium ROI	2.79–4.25°N, 274.94–276.93°W	144–687	9.7–18.9%	Figures 4–5
Small ROI	2.81–4.47°N, 274.97–275.76°W	144–687	10.5–20.7%	Figures 4 and 5
Image pair #1[e]	I01395005, I19050003	116–696		Figure 9
		Argyre Planitia		
Single ROI	42.96–47.45°S, 28.68–34.51°W	25–572	6.4–15.7%	Figure 6
Image pair #1	I41921002, I34365010	215–918		Figure 13
		Terra Cimmeria		
Large	24.46–26.57°S 206.59–208.37°W	165–554	7.6–9.8%	Figure 16
Small	26.20–26.60°S 206.83–207.30°W	203–412	9.4–13.5%	Figure 16
Image pair #1	I51665002, I08440010	145–410		Figure 17

[a] ROIs indicate TES analyses; image pairs indicate THEMIS analyses.

[b] In SI units J-m^{-2} K^{-1}.s$^{-1/2}$.

[c] Average olivine range not reported for THEMIS images as those abundances represent olivine-bearing surfaces which may contain other phases besides olivine.

[d] Only data from all-season analysis are reported.

[e] Only data from analysis without noise-removal filter are reported.